A somatic afterhyperpolarization is driven by ion channel nodes across a Spectrin Polygonal Lattice

Giriraj Sahu[†1], Dylan Greening[δ#1], Xiaoqin Zhan[θδ], Wilten Nicola[ϒδ] and Ray W. Turner[θδ*]

Author Footnotes: 1 These authors contributed equally.

[†]Molecular Biophysics Unit, Indian Institute of Science, Bangalore-560012, India, [θ]Department Clinical Neuroscience,[ϒ]Department Cell Biology & Anatomy, [δ]Hotchkiss Brain Institute, #Snyder Institute for Chronic Diseases, Cumming School of Medicine, University of Calgary, Calgary, Alberta, Canada T2N 4N1,

Running title: A Spectrin Polygonal Lattice defines sAHP nodes

Figures: 7
Supplementary Figures: 10
Supplementary Tables: 5

Key words: slow AHP, hippocampus, Cav1, KCa3.1, RyR2, spectrin, cytoskeleton, ER-PM junction

*** Corresponding Author:**
Ray W. Turner
Health Research Innovation Ctr 1AA14
3330 Hospital Dr. N.W.
University of Calgary, Calgary, Alberta
Canada T2N 4N1
(403) 220-8452
FAX (403) 210-7446
Correspondence: rwturner@ucalgary.ca

Declaration of Interests:
The authors declare no competing interests.

Abstract 149 words
A spectrin-actin Membrane Periodic Skeleton defines the distribution of ion channels that support spike conduction down axons, but it is not known how calcium and potassium channels are organized at the soma to control spike output patterns. The hippocampal pyramidal cell slow AHP is generated by a CaRyK protein complex of Cav1.3 calcium, RyR2, and IK potassium channels. Super resolution imaging and dimension reduction identified a highly organized distribution of CaRyK proteins across the spectrin cytoskeleton. Rows of CaRyK protein clusters with 150 nm periodicity extended to branchpoints to align with a non-rigid lattice-like structure of spectrin βII and the actin linking proteins actinin I and II. The slow AHP was highly dependent on the integrity of the spectrin cytoskeleton that colocalized CaRyK proteins. The data indicate that the somatic slow AHP is generated by CaRyK proteins distributed as functional ion channel nodes across a Spectrin Polygonal Lattice.

Introduction (516 words)
Intrinsic ionic mechanisms at the level of neuronal somata integrate synaptic inputs to shape spike output. Central to this process are calcium and calcium-gated potassium channels that generate the afterhyperpolarizations (AHPs) that pattern spike output into bursts and pauses. Yet the mechanisms by which calcium and potassium channels are spatially organized to control spike output remains to be determined. In hippocampal neurons a triprotein complex comprised of Cav1.x calcium channels, ryanodine receptor 2 (RyR2), and KCa3.1 (IK) potassium channels (CaRyK complex) formed at ER-PM junctions contributes to generating a slow AHP of several seconds duration (King *et al*, 2015; Sahu *et al*, 2019; Sahu & Turner, 2021; Sahu *et al*, 2017; Turner *et al*, 2016; Tiwari *et al*, 2022, 2018, 2019). The factors that govern expression of the CaRyK complex are important as the slow AHP controls spike output in normal and disease states, and circuit function with age (Tiwari *et al*, 2019; Sahu & Turner, 2021; Moore *et al*, 2023).

It is known that efficient propagation of spikes from the axon initial segment (AIS) and down an axon depends on the precise localization of sodium and potassium channels (Trimmer, 2015; D'Este *et al*, 2017; Zhou *et al*, 2022). It was recently shown that axons exhibit a Membrane Periodic Skeleton (MPS) where lengths of spectrin running parallel to the axon support periodic circumferential bands of actin (Han *et al*, 2017; Xu *et al*, 2013; Zhong *et al*, 2014; D'Este *et al*, 2015; Unsain *et al*, 2018; Zhou *et al*, 2022; Lorenzo *et al*, 2023). Sodium and potassium channels are localized by linking to the MPS with a semi-periodic "1D" distribution (Unsain *et al*, 2018; Xu *et al*, 2013; D'Este *et al*, 2017; Zhou *et al*, 2022; Maverick & Tamkun, 2022). By comparison, a "2D" configuration of spectrin with a polygonal-like organization was reported over select regions of the soma or proximal dendritic membranes (Zhong *et al*, 2014; Han *et al*, 2017). It is not known if spectrin plays a role in coordinating the somatic expression of a CaRyK complex that underlies the slow AHP.

We used super resolution microscopy and dimension reduction to assess the spatial distribution of the CaRyK complex and its relationship to the cytoskeleton at the soma of hippocampal neurons. Calculations of nearest neighbour distance (NND) or non-negative matrix factorization (NMF) revealed a coordinated distribution of immunolabel for CaRyK complex proteins across the entire somatic surface. One was a linear series (row) of up to 8 punctate clusters with a periodicity of ~155 nm that could reach and extend beyond branch points, and a second at distances of ~600-800 nm. Together these clusters established a lattice-like structure that was shared with that of spectrin βII and actinin linking proteins that colocalized with CaRyK complex proteins. Even moderate disruption of spectrin cytoskeletal organization by calpain-mediated proteolysis reduced the colocalization of spectrin and IK proteins and decreased the

sAHP in CA1 hippocampal neurons. Together these data reveal a high degree of spatial organization of the CaRyK complex across the soma in relation to a cytoskeletal Spectrin Polygonal Lattice that is important to generation of the sAHP.

Results

STORM-TIRF imaging was used to localize CaRyK complex proteins within 150 nm of the coverslip surface of MAP-2 positive cultured neurons. Images were defined with 10-25 nm localization precision of individual fluorophore centroids. Immunolabels were not assumed to reflect individual ion channels, with a group of fluorophore labels defined by STORM referred to only as clusters (Sahu *et al*, 2019; Higham *et al*, 2019). Cluster analysis was performed using masks that included the lateral membrane borders and entire surface of somatic membrane, but not dendritic or axonal processes outside of this region. For STORM-TIRF images, nearest neighbour distance (NND) and non-negative matrix factorization (NMF) calculations were applied to typically >500 clusters per label/cell (675 ± 26; n = 279) and up to 43,000 clusters in up to 55 cells per label for statistical analyses.

CaRyK complex proteins exhibit a high degree of organization across somatic membrane

STORM-TIRF imaging of immunolabels for proteins that comprise the CaRyK complex revealed discrete labeling of clusters across the entire somatic membrane (***Fig. 1 and 3***). We first focused on cells dual labeled for Cav1.3 and IK immunofluorescence. An extensive distribution of clusters could be detected across large fields of view (***Fig. 1A***) or in magnified ROIs (***Fig. 1B***) as punctate labels in isolation or with discrete overlap of the alternate fluorophore. A distinct pattern was apparent for both IK and Cav1.3 as closely spaced (rows) of clusters (***Fig. 1B***), where ~50-60% of clusters were contained within rows of 3, ~20-25% of clusters in rows of 4, and only a few percent in rows of up to 8 clusters (***Fig. 2A***). Rows of clusters could further meet at junction points (***Fig. 1B***) from which 1-2 branches of similarly spaced rows of clusters extended at angles of 70-150 degrees (Cav1.3, 118 ± 2.33 degrees, n = 103; IK, 120 ± 1.59 degrees, n = 101) (***Fig. 2B***). Either IK or Cav1.3 could present as a dominant label, as rows of clusters could be detected for either IK or Cav1.3 (***Fig. 1B*,** ROI-3 and 4), with overlap or close association of the other cluster label along a row or at discrete sites that could include the junction point (***Fig. 1B*,** ROI-4 and 6). Clusters of immunolabel could also be detected as being physically isolated from cluster rows with or without close apposition of the alternate label (***Fig. 1B,*** ROI-5-7).

NND calculations identified two inter-cluster relationships for both IK and Cav1.3 (***Fig. 1, C and D***). For IK clusters one was fit over a short distance of <500 nm (median of 177 nm), and a second over a larger range of ~300-2000 nm (median, 699 nm) (***Fig. 1C***). A similar dual distribution of minimal distance was apparent between Cav1.3 clusters up to ~400 nm (median, 169 nm) and ~200-2000 nm (median, 664 nm) (***Fig. 1D, Supplementary Table S1***). A plot of the minimal distance between neighboring IK and Cav1.3 clusters instead revealed a single right-skewed histogram of less than ~1000 nm (median, 188 nm) (***Fig. 1E***). These data are important in confirming a nanometer association between Cav1.3 and IK clusters consistent with colocalization (Sahu *et al*, 2019; Higham *et al*, 2019), and two common patterns in the minimal distance between IK and Cav1.3 immunolabels.

Detecting patterns of protein distribution

The ability to consistently define two patterns of cluster distances between Cav1.3 and IK immunolabels suggests a non-random distribution of CaRyK complex proteins across the somatic membrane. To test this we randomized the centroid positions for each of the CaRyK protein data sets. These tests returned

unimodal histograms consistent with spatially random data that were distinct from those of experimental data (***Fig. S1***).

To more fully assess the spatial organization of these labels we conducted NMF analysis to extract the top 6 detectable features of immunolabel clusters in each cell for analysis (see Materials and Methods, ***Fig. S2-S5***). A key advantage to NMF is the ability to define features, in an unsupervised fashion, beyond the minimal nearest neighbor for every cluster centroid without the need to identify the specific orientation of Regions of Interest (ROI) (Berry *et al*, 2007). As a crosscheck of this approach we compared NMF to the alternate method of autocorrelation applied to predefined ROIs for spectrin βII in the MPS in axons and dendrites and obtained very similar spatial separations of ~155 nm (***Fig. S4***). It is of interest that these values are somewhat shorter than previous reports of an average value of ~180-190 nm (Han *et al*, 2017; Xu *et al*, 2013; D'Este *et al*, 2017). We consider this to reflect the elasticity inherent to a resting spectrin framework (Leterrier & Pullarkat, 2022; Brown *et al*, 2015), or potentially the relative length of spectrin subunits incorporated into the developing cytoskeleton at ~DIV 10-15 (Han *et al*, 2017; Machnicka *et al*, 2012; Zhong *et al*, 2014; Huang *et al*, 2017) (see Discussion).

We therefore used NMF as an objective, automated process to define meaningful patterns of immunolabel clusters at the soma. To identify relationships between colocalized clusters (Sahu *et al*, 2019), we restricted NMF analysis to only the centroids of clusters identified to exhibit overlap in fluorescence between the two labels (***Fig. S6***).

CaRyK complex proteins exhibit a regular pattern of expression

IK and Cav1.3

NMF was applied to IK and Cav1.3 clusters to assess the periodicity of rows of clusters as well as isolated clusters. Features extracted by NMF analysis that reflected a row of clusters were fit by a damped oscillatory model to identify a period for IK clusters of 139 nm (***Fig. 1F, Supplementary Table S2***). Features with a repeating series of Cav1.3 clusters exhibited a period of 159 nm (***Fig. 1G***). When comparing the relationship between colabeled IK-Cav1.3 clusters, NMF reported a regularity with a period of 156 nm (***Fig. 1H***). To define potential patterns in the distant (isolated) group identified through NND calculations (***Fig. 1, C and D***), we extracted features with peaks separated by distances of 375-1506 nm. This second group of features could be described with a single gamma fit, returning median values of 679 nm for isolated IK-IK clusters, 638 nm for Cav1.3-Cav1.3 clusters, and 795 nm for colabeled IK-Cav1.3 isolated clusters *(**Fig. 1I-K***).

These tests established a high degree of shared spatial regularity of IK and Cav1.3 labels as rows of tightly spaced clusters ~140-160 nm apart or as isolated clusters separated by ~600-800 nm (***Supplementary Table S2***). A colocalization of immunolabels for IK and Cav1.3 could be detected for both rows and isolated clusters of distribution.

RyR2 relationship to Cav1.3 and IK

Previous work established that RyR2s are colocalized with nanometer proximity to Cav1.3 and IK channels as part of a CaRyK complex at ER-PM junctions (Vierra *et al*, 2019; Sahu *et al*, 2019; Vierra & Trimmer, 2022; Sahu & Turner, 2021). Immunolabeling confirmed extensive colocalization of these labels and a similar spatial organization of RyR2 across the soma (***Fig. 3A-D)***. RyR2 clusters could thus be visually distinguished as rows of 3-8 clusters that converged at branch points from which other rows of clusters labeled for RyR2 and/or the counter-labeled protein could extend (mean angle, 116 ± 1.51 degrees, n = 100) (***Fig. 2C and D, 3B and D***). RyR2 clusters could also be identified in isolation with or

without overlap of an ion channel fluorophore emission suggestive of colocalization (***Fig. 3, B and D***). The latter results are important in emphasizing that RyR2 labeling was not obligatory with Cav1.3 or IK labeling but could exhibit a high degree of co-organization in expression within the 150 nm distance from the surface of the coverslip defined by TIRF imaging.

NND analysis confirmed a separation of RyR2 cluster distances into one group with a nearest neighbor median distance of 185 nm and a more dispersed group (median, 755 nm) (***Fig. 3E***). NND calculations between RyR2 clusters and those for Cav1.3 or IK channels returned right-skewed interval histograms for both RyR2-Cav1.3 and RyR2-IK (medians, 238 nm) (***Fig. 3, F and G***). NMF analysis further revealed a high degree of spatial organization for RyR2, where repeating clusters were fit with a period of 158 nm for both RyR2-RyR2 and RyR2-Cav1.3 clusters, and 123 nm for RyR2-IK clusters (***Fig. 3H-J***). The spatial relationship between isolated clusters for RyR2 was again fit with larger median values for RyR2-RyR2 (689 nm), RyR2-Cav1.3 (819 nm), and RyR2-IK (810 nm) (***Fig. 3K-M***). Altogether these analyses confirmed a close spatial relationship between RyR2 and CaRyK complex ion channels that co-distributed as either rows of clusters or isolated clusters.

The spatial distribution of CaRyK complex proteins reflects coassociation with the spectrin cytoskeleton

The organized expression of CaRyK complex proteins across the somatic membrane imply the presence of an underlying mechanism for organization. It is known that the spatial distribution of sodium and potassium channels in axons and portions of dendrites is determined by a "1D" spectrin-actin-based MPS (Han *et al*, 2017; Xu *et al*, 2013; Zhong *et al*, 2014; D'Este *et al*, 2015; He *et al*, 2016; D'Este *et al*, 2016; Zhou *et al*, 2022). Evidence further points to a "2D" structure formed by spectrin in the somatic region (Han *et al*, 2017). Several isoforms of spectrin are expressed in neurons (Machnicka *et al*, 2012; Unsain *et al*, 2018; Lorenzo *et al*, 2023) with the extent of a 1D structure in dendrites related to the level of spectrin βII (Zhong *et al*, 2014; Han *et al*, 2017). We thus used labeling for the C-terminus of spectrin βII for STORM-TIRF measures of any spatial relationship with respect to CaRyK complex proteins at the soma.

Spectrin βII and CaRyK complex proteins

We found that spectrin βII immunolabel could be visualized over the entire region of hippocampal neuron somata (***Fig. 4***). As found for CaRyK complex proteins, punctate clusters of spectrin βII were detected aligned in rows that reached branch points where 1 or 2 rows of clusters extended at angles with a mean of 118 ± 1.63 (n = 104) (***Fig. 2C and D***), or as isolated clusters (***Fig. 4A-D***). In dual labeled cells spectrin βII and Cav1.3 exhibited close alignment that resulted in overlap or close apposition of fluorophore emissions (***Fig. 4, C and D***). In some cases the labels were complementary such that labeling of rows of either spectrin βII or Cav1.3 clusters could effectively bridge a row of labels towards an apparent branch point (***Fig. 4D***).

Quantitative analyses revealed many similarities in these patterns of distribution for spectrin βII and Cav1.3 labeling. NND calculations between spectrin βII clusters revealed two populations with short inter-cluster distances of less than ~400 nm (median, 176 nm), and a second broader distribution up to ~2000 nm (median, 733 nm) (***Fig. 4E***). The NND histogram between spectrin βII and Cav1.3 clusters was right-skewed with a median of 288 nm, indicating a preferred close spatial relationship (***Fig. 4F***). NMF analysis of spectrin βII - spectrin βII clusters identified a periodicity of 159 nm in the soma (***Fig. 4G***), similar to that determined for spectrin βII clusters in neural processes (see ***Fig. S4***). Cells co-labeled

for spectrin βII and Cav1.3 also identified a regularity in overlapping labels at the soma with a period of 134 nm *(**Fig. 4H**)*. NMF applied to isolated clusters identified distances of 746 nm between spectrin βII clusters and 917 nm for spectrin βII-Cav1.3 clusters (***Fig. 4J***).

Immunolabeling for spectrin βII and either IK or RyR2 revealed similar relationships in organization as that for Cav1.3 (***Fig. 5A-D***). In dual-labeled cells, NND calculations revealed two populations for each of spectrin βII and RyR2 clusters, with an early peak and another with a broader distribution (***Fig. S7***). By comparison, NND analysis returned right-skewed histograms for spectrin βII-IK (median, 238 nm) and spectrin βII-RyR2 (median, 288 nm) (***Fig. 5, E and F***). NMF analysis of colabeled clusters identified a regular distribution of rows of clusters for spectrin βII-IK (period, 121 nm) and for spectrin βII-RyR2 clusters (period, 160 nm) (***Fig. 5, G and H***), and for isolated clusters longer median values for spectrin βII-IK (median, 743 nm) and spectrin βII-RyR2 (median, 889 nm) (***Fig. 5, I and J***).

These data are important in revealing that the spatial organization found for each of the three subunits of the CaRyK complex essentially match that of spectrin βII as an indicator of the underlying cytoskeleton.

Actinin I and II linking proteins

Ion channels in the membrane connect to the actin-spectrin cytoskeleton through intermediate linking proteins (Liem, 2016). Key to this are actinins that form extended rod-shaped molecules that cross-link actin filaments, which in turn connect to spectrin (Liem, 2016). Previous work has uncovered roles for actinin I and II in controlling the organization of ion channels, including those relevant to subunits in the CaRyK complex (Hall *et al*, 2013; Lu *et al*, 2007; Sadeghi *et al*, 2002; Turner *et al*, 2020; Lu *et al*, 2009; Zuccotti *et al*, 2011; Hiess *et al*, 2015).

Actinin proteins and the CaRyK complex: Initial tests confirmed a shared spatial organization for spectrin βII and either actinin I or actinin II proteins dual labeled in hippocampal neurons, as confirmed by NND and NMF calculations (***Fig. S8, S9***). We then examined the spatial relationship between CaRyK complex proteins and actinin I and actinin II. Dual labeled images indicated a very tight association between clusters for actinins and each of Cav1.3, IK, or RyR2 (***Fig. 6A-F***). Immunolabeled clusters were distributed in tightly spaced rows that exhibited strong overlap or alternation in segments of cluster labels between actinin I and Cav1.3, actinin II and IK, and actinin II and RyR2 (***Fig. 6B, D, and F***). Indeed, the extent of colabeling of actinin II cluster rows with IK or RyR2 provided some of the clearest indications of expression consistent with an underlying spectrin-based architecture (***Fig. 2C and D, 6C-F***) *(Lu et al, 2009; Hall et al, 2013)*. NND analysis restricted to clusters of actinin and CaRyK complex proteins presented interval histograms that were strongly right skewed, with median values between different pairs of clusters ranging from 138-213 nm (***Fig. 6G-I***). NMF analysis also confirmed a periodicity of 147-160 nm between colabeled actinin - CaRyK complex proteins, and for isolated clusters of 730-790 nm (***Fig. 6J-O***).

Dependence of CaRyK complex organization on the spectrin cytoskeleton

The spatial arrangement of interacting proteins strongly suggests a spectrin-based determination of CaRyK complex organization. We thus tested if disrupting the spectrin cytoskeleton would affect CaRyK complex organization and the sAHP. Maitotoxin (MTX) is a potent marine toxin that activates intrinsic calcium channels to increase internal calcium to levels that activate calpain to proteolyse spectrin αII (Löfvenberg & Backman, 1999; Wang *et al*, 1996; Zhang *et al*, 2009; Glantz *et al*, 2007; Czogalla & Sikorski, 2005). MTX has been shown to invoke a concentration- and time-dependent proteolysis of spectrin subunits, with breakdown products (bdps) for spectrin αII evident following treatment with 1 nM

MTX for 1-2 hr (Löfvenberg & Backman, 1999; Wang *et al*, 1996; Zhang *et al*, 2009; Glantz *et al*, 2007; Czogalla & Sikorski, 2005).

To validate this we tested for spectrin αII bdps on Western blots prepared from hippocampal tissue slices exposed to 1 nM MTX for 2 hrs in normal aCSF (**Fig. 7A**). Interestingly, a moderate level of spectrin αII bdps was evident in resting conditions, indicating some breakdown of spectrins during slice preparation or recovery (**Fig. 7A; *Fig. S10***). MTX treatment induced a 2 fold increase of spectrin αII bdps with a primary band at ~150 kDa that was greatly diminished by pretreatment with 5 µM calpeptin as a calpain blocker (**Fig. 7A; *Fig. S10***).

We next tested if MTX treatment could affect the spatial organization of spectrin and CaRyK complex proteins in CA1 pyramidal cells of intact adult tissue sections. For this we used 2D STED to calculate NND and the degree of association between spectrin αII and IK as a representative CaRyK complex protein. We also applied a relatively mild exposure of 80 pM MTX for 1 hr as this was just on the threshold for affecting general cell health during recordings, but produced detectable levels of bdps on western blots. Tissue sections from P21-26 rat hippocampus were prepared and subjected to MTX with or without calpeptin. Imaging was restricted to single optical sections near the membrane surface of optical image stacks with MAP2 as a cytoplasmic marker to help define cell boundaries. NND calculations for STED spectrin αII images were applied to typically >100 clusters per cell (350 ± 25; n = 37) and for IK > 70 clusters per cell (229 ± 19; n = 37).

In the somatic region of CA1 pyramidal cells of control tissue, calculation of NND values for all spectrin αII-IK clusters returned a right-skewed histogram with 255 nm median value (**Fig. 7B, C**). Restricting analysis to only those clusters exhibiting direct pixel overlap (colocalized) also returned histograms best fit by two exponentials with median values of 174 nm and 462 nm (**Fig. 7B**). MTX treatment at 80 pM for 1 hr increased the median NND value and broadened the distribution of intervals, confirming a trend in the action of MTX at the population level without excess disruption of the spectrin cytoskeleton (**Fig. 7B, C**). Pretreatment with calpeptin substantially narrowed the distribution of intervals (**Fig. 7B**), revealing the extent of action of calpain under normal conditions *in vitro*. By comparison, NND calculations for spectrin αII and IK clusters exhibiting direct pixel overlap indicated a substantial drop in the peak probability of NND values in the group of nearest neighbors, and >30% increase in histogram median values with incorporation of longer NND intervals (**Fig. 7B**). Most striking was a dramatic reduction (~60%) in the total number of clusters exhibiting colocalization, revealing a progressive dissociation of spectrin αII and IK proteins (**Fig. 7C**). Pretreatment with calpeptin prevented these effects of MTX on NND measures and the number of colocalized clusters (**Fig. 7B, C**).

The sAHP of CA1 pyramidal cells depends on the integrity of the spectrin cytoskeleton

The IK-mediated sAHP of CA1 pyramidal cells is known to depend on junctophilin proteins that link the membrane and ER-associated proteins of the CaRyK complex (Sahu *et al*, 2019; Sahu & Turner, 2021). To determine if generation of the sAHP is dependent on CaRyK complex protein expression with respect to an intact spectrin framework, we recorded the sAHP evoked in P20-25 rat CA1 pyramidal cells in *in vitro* tissue slices to define the effects of MTX on the sAHP. Under control conditions the peak amplitude of the IK-mediated sAHP current (IsAHP) was 92.5 ± 12.3 pA (n = 8; - 50 mV) (**Fig. 7D**). Pretreatment with calpeptin (5 µM, 1 hr) had no significant effect on IsAHP amplitude (**Fig. 7D**). We noted a high sensitivity of pyramidal cells to the toxin, with unacceptable leak currents (2 - 3 nA) when slices were pretreated with 200 pM to 1 nM MTX (1-2 hr). With 40 pM MTX pretreatment for 1-2 hr, cells maintained key aspects of health, including leak currents < 80 pF and resting potentials comparable to

untreated cells (Control, 69.6 ± 1.2 mV, n = 8; MTX, 67.1 ± 0.6 mV, n = 9; $p > 0.05$). However, the IsAHP peak amplitude was significantly reduced after MTX treatment to 58.4 ± 5.9 pA (control 92.5 ± 12.3 pA, n = 8; $p < 0.05$), an action that was blocked by calpeptin (5 μM) when present before and during MTX exposure (84.0 ± 5.6 pA, n = 10; $p > 0.05$) (**Fig. 7D**). Together these data indicate that the sAHP depends on the colocalization of IK as a CaRyK complex protein with the structural framework provided by spectrin isoforms across the soma.

Discussion

The mechanisms that define the expression of membrane ion channels and the protein-protein interactions needed to create complex patterns of neuronal output has been a long-standing area of investigation. It has now been established that spike propagation down an axon is enabled by a spectrin-actin MPS that enables a highly ordered arrangement of sodium and potassium channels at nodes of Ranvier (Unsain *et al*, 2018; Xu *et al*, 2013; D'Este *et al*, 2017; Zhou *et al*, 2022; Maverick & Tamkun, 2022). Yet the pattern and frequency of spikes are instead controlled by ion channels at the *soma* that use changes in calcium concentration to modify their level of activation. Specialized ER-PM junctions where the ER reaches to within 15 nm of the somatic plasma membrane can coordinate activity of ion channels and internal calcium release sites to control cell excitability (Dixon & Trimmer, 2023; Fox *et al*, 2015). One representative assembly at ER-PM junctions is the CaRyK complex that contributes to generating a slow AHP in hippocampal neurons (Sahu *et al*, 2019; Sahu & Turner, 2021; King *et al*, 2015; Wang *et al*, 2016; Turner *et al*, 2016; Higham *et al*, 2019). The current study reveals that proteins of this CaRyK complex are not randomly distributed at the soma. Rather, the CaRyK complex exhibits a coordinated distribution across the somatic surface consistent with a spectrin-based cytoskeletal matrix (Han *et al*, 2017). Moreover, even modest disruption of the spectrin framework by calpain is sufficient to reduce spectrin αII-IK colocalization and substantially reduce the sAHP in whole-cell recordings. Thus, the functional organization of CaRyK complex proteins required to generate an sAHP depends on the spectrin cytoskeletal matrix.

Patterns of organization of the CaRyK complex

STORM-TIRF images revealed that CaRyK proteins are distributed in patterns with a periodicity defined through NND and NMF analyses that reflects a polygonal organization at the soma. We thus identified rows of immunolabels composed of ~3-8 clusters spaced ~155 nm apart for each of the CaRyK complex proteins. The rows of clusters further reached branchpoints from which additional rows of clusters extended at internal angles of 60-150 degrees (mean of 118 degrees) that could effectively close loops in the branching structure. A second prominent pattern for CaRyK proteins and spectrin βII was in isolated clusters with a peak distance of ~600-800 nm. We note that the clusters identified using STED in P20-25 neurons also exhibited NND values of ~174 nm and a second at ~450-500 nm, confirming these distributions in both cultured cells and normally developed CA1 pyramidal cells. It needs to be considered that Kv2.1/2.2 potassium channels have been shown to control assembly of calcium channels and RyRs at ER-PM junctions (Lim *et al*, 2000; Antonucci *et al*, 2001; Vierra *et al*, 2019; Mandikian *et al*, 2014; Johnson *et al*, 2019; Fox *et al*, 2015; Dixon & Trimmer, 2023). At this time we do not know the extent to which Kv2.x channels are responsible for organizing either of the patterns observed here for subunits of the CaRyK complex.

Spectrin-based cytoskeletal matrices

The close association of CaRyK complex proteins with the branching architecture of spectrin βII and associated actinin proteins suggest a key role for the spectrin cytoskeleton. The MPS of axons, the AIS, and some dendrites reflect a "1D" pattern of longitudinally oriented spectrin repeats and circumferential bands of actin at regularly spaced intervals (Han *et al*, 2017; Xu *et al*, 2013; Zhong *et al*, 2014; D'Este *et al*, 2015; Zhou *et al*, 2022; Lukinavičius *et al*, 2014; Lorenzo *et al*, 2023; Rentsch *et al*, 2024). The somatic surface of neurons has instead been reported to exhibit a 2D structure of spectrin labeling that undergoes an increase in complexity over time to reach ~45% of cell surface area by DIV 28 (Han *et al*, 2017). The current work employed dimension reduction techniques to objectively define a polygonal architecture assembled from spectrin isoforms across the somatic surface. This structure is then conferred through linking proteins (actinin I and II) to the expression pattern of a membrane protein complex with a direct role in shaping the pattern of spike output. Our measures of the distance between spectrin repeats at the soma using an antibody against the C terminus of spectrin βII was fit by an oscillatory model at ~159 nm ($R^2 = 0.92$) in dissociated neurons and with NND for spectrin αII in adult neurons to 174 nm ($R^2 = 0.94$). This compares to reported values of the distance between spectrin repeats in the MPS of unmyelinated axons of 182 ± 16 nm (range of 150-220 nm) (Xu *et al*, 2013) and for myelinated axons of 180 ± 35 nm (range of 80-240 nm) (D'Este *et al*, 2015). The range of values we obtained would be consistent with the known elasticity of spectrin when in a resting state (Lux, 2016; Grum *et al*, 1999; Zhou *et al*, 2022; Leterrier & Pullarkat, 2022). We note that the matrix-like branching structure for labels tested here bears a striking resemblance to the polygonal structure naturally adopted by spectrin in structures like that defined in erythrocyte membranes (Nans *et al*, 2011; Lux, 2016; Lorenzo *et al*, 2023). While the erythrocyte spectrin cytoskeleton is often referred to as pseudohexagonal, the organization detected at the soma of hippocampal pyramidal cells could be described as a non-rigid lattice assembled from 3-6 edges between lattice points that we refer to as a Spectrin Polygonal Lattice (SPL). Compared to the linear MPS structure that is ideal to support the extension of an axon or dendrite, the natural process of spectrin adopting an SPL configuration presumably reflects the need to provide flexible support for a larger surface area and the rounded structure of neuronal somata. It further serves to create attachment points for an ion channel complex associated with ER-PM junctions.

ER-PM junctions as ion channel nodes

ER-PM junctions have previously been shown to coordinate functional outcomes that include endo- and exocytosis, calcium rebalancing, membrane protein delivery, lipid transfer, and excitation-transcription coupling (Deutsch *et al*, 2012; Antonucci *et al*, 2001; Fu *et al*, 2017; Leung *et al*, 2003; Vierra & Trimmer, 2022; Vierra *et al*, 2021). ER-PM junctions can also coordinate the expression of calcium channels at the plasma membrane and RyRs in the ER (Vierra *et al*, 2019; Sahu *et al*, 2019; Fox *et al*, 2015; Johnson *et al*, 2019; Dixon & Trimmer, 2023). The combination of Cav1.3-RyR2-IK proteins studied here as component elements of ER-PM junctions are necessary for the generation of a slow AHP (Sahu *et al*, 2019; Sahu & Turner, 2021; Sahu *et al*, 2017). Spikes near the soma can thus regulate firing rate by activating calcium increases to produce a slow AHP of up to secs duration. The current work highlights how the CaRyK complex exhibits a lattice-like organization that follows the spectrin-based architecture. Even modest activation of calpain by MTX decreased the colocalization of spectrin and IK immunolabels and reduced the amplitude of the sAHP. The data would then support a role for ER-PM junctions (Dixon & Trimmer, 2023) as ion channel nodes that colocalize calcium- and calcium-gated potassium channels at the soma with a spatial distribution defined by the spectrin cytoskeleton. When assembled and distributed in this manner, calcium entry and/or internal calcium release can trigger the calcium-activated potassiums

required to regulate the frequency and pattern of spike output. The MPS of axons is instead tailored to organize sodium and potassium channels for the efficient propagation of spikes from the soma to postsynaptic structures.

It will be interesting to determine if other functionally coupled calcium-potassium channel pairs (Andrade *et al*, 2012) also coordinate their activity at ER-PM junctions to influence spike output. The CaRyK complex defined here reflects a functional coupling between IK channels and two calcium sources that contribute to generating the slow AHP in CA1 pyramidal cells (Sahu & Turner, 2021). While the expression of IK channels in central neurons was initially debated, the role for IK channels in generating a slow AHP or modulating cell output has now been established in numerous cell types, including CA1 hippocampal pyramidal cells (King *et al*, 2015; Sahu *et al*, 2019; Sahu & Turner, 2021; Sahu *et al*, 2017; Turner *et al*, 2016; Higham *et al*, 2019; Tiwari *et al*, 2022, 2018; Charlick *et al*, 2024; Tiwari *et al*, 2019), cerebellar Purkinje cells (Engbers *et al*, 2012; Gründemann & Clark, 2015), pyramidal cells in the visual and entorhinal cortices (Roshchin *et al*, 2020; Oblasov *et al*, 2024), GnRh cells (Constantin *et al*, 2024), and rod bipolar cells (Park *et al*, 2025). The current work is important in showing how a CaRyK complex in CA1 hippocampal pyramidal cells is organized across the soma and that sAHP amplitude is highly dependent on the spectrin cytoskeleton. The extent to which the sAHP in other cells depends on a similar protein complex distributed with respect to the spectrin cytoskeleton remains to be determined.

Limitations of the current study

We note that the extent to which we could define the full structure of a spectrin-based cytoskeleton was limited by several factors. For one, neurons are known to express tetramers of α and different β spectrin subunits (Unsain *et al*, 2018; Gao *et al*, 2011; Zhou *et al*, 2022; Lorenzo *et al*, 2023). Our labeling and NMF calculations centered on the spectrin βII C terminus and were restricted to dual labeled protein pairs exhibiting overlapping fluorescent emissions, reducing the total number of clusters that might align in a given sequence. For these reasons the full extent of a spectrin-based polygonal structure was likely underestimated.

Materials and Methods

Experimental Design

The objective of this study was to use super resolution STORM-TIRF imaging of immunolabels for a CaRyK protein complex in relation to markers of the cytoskeleton at the soma of hippocampal pyramidal cells in dissociated cultures. Dimension reduction approaches were used to objectively quantify the physical relationship and patterns of CaRyK protein immunolabels in relation to spectrin. STED imaging in intact tissue slices was used to quantify nearest neighbor distance to define the dependence of the spectrin framework on generating a slow AHP in CA1 pyramidal cells.

All materials and supplies with catalog numbers, software, and site of data repository are provided in ***Supplementary Table S5.***

Animals

Timed pregnant Sprague Dawley rats were obtained (Charles River) and maintained for at least 7 days

after shipping according to the guidelines of the Canadian Council of Animal Care and experimental protocols approved by the University of Calgary Animal Care Committee.

Dissociated hippocampal cell cultures

P0-P1 male or female rat pups were used to prepare low-density dissociated cultures of rat hippocampal neurons (Sahu *et al*, 2017, 2019). P0-P1 rat pups were anesthetized on ice for 3-5 min and hippocampi dissected and dissociated by papain treatment followed by titration with progressively smaller bore glass pipettes. After each titration step the supernatant containing the cells was passed through a 70 µm separation filter (Corning, Cat. 07201431) into a 50 ml tube. Cells were centrifuged at 300 x g for 10 min and the supernatant completely aspirated and resuspended in MACS buffer (cat#130-091-221) (diluted 1:20). Unlabelled hippocampal neurons were collected using a MiniMACS™ Separator (130-042-102). Prior to collection, cells were incubated with anti-rat CD11b/c antibody (Cat#130-105-634) conjugated to magnetic microbeads. After microglia depletion, cells were incubated with GLAST (ACSA-1)-biotin (Cat#130-095-826) according to manufacturer instructions (Miltenyi Biotec, CA) (***Supplementary Table S5***) (Marek *et al*, 2008). Collected unlabeled neurons were diluted in basal neural medium (BME) supplemented with 1 mM Na-pyruvate, 2 mM L-glutamine, 10 mM HEPES, 1% B-27 supplement, 5% FBS, 0.6% glucose, and 1% penicillin-streptomycin for correct plating density. The cell suspension was then plated on laminin and poly-l-lysine-coated glass coverslips in 12 well culture dishes at 3500–5300 cells/cm^2. Cells were grown on 18 mm No 1.5 coverslips (Electron Microscopy Sciences, PA) at 37 ºC for three days in BME, followed by exchange with BME lacking FBS. Culture medium was refreshed with BME lacking FBS every three days. Cultured hippocampal neurons at 10-15 days *in vitro* (DIV 10-15) were used to obtain images of isolated neurons to further reduce the risk of glial membrane envelopment that could interfere with imaging neuronal proteins adjacent to the coverslip surface.

***In vitro* tissue slices:**

P21-26 male Sprague Dawley rats were anesthetized by isoflurane inhalation until unresponsive to tail pinch and transcardially perfused with ice-cold sucrose medium (mM) 2.5 KCl, 0.5 $CaCl_2$, 1.25 NaH_2PO_4, 3 $MgCl_2$, 25 $NaHCO_3$, 20 D-Glucose, 215 sucrose bubbled with carbogen (95% O_2 and 5% CO_2) gas. The brain was dissected out and blocked and mounted in a Leica Vibratome (Leica VT1200S) to cut 300 µm slices in ice cold artificial cerebrospinal fluid (aCSF) composed of (mM): 125 NaCl, 25 $NaHCO_3$, 3.25 KCl, 1.5 $CaCl_2$, 1.5 $MgCl_2$, 25 D-Glucose bubbled with carbogen (95% O_2 and 5% CO_2) gas. Tissue slices then recovered for 20 - 30 min at 35 ºC before storing at room temperature (RT, 22ºC) in carbogen-bubbled aCSF prior to recordings. For patch-clamp recordings, slices were treated with 40 pM Maitotoxin (MTX, BOC Sciences, NY) in aCSF for 1-2 hr with or without 1 hr pretreatment and continued exposure to 5 µM calpeptin (ThermoFisher, ON). Since calpeptin stocks were prepared in DMSO, a final concentration of 0.2% DMSO was used to treat control sections. Based on observations from Western blotting, DMSO did not change the ratios of spectrin αII or βII breakdown products (bdps) in control sections when compared to untreated ones.

Protein Biochemistry: After dissection and mounting for vibratome sectioning (as above), tissue slices destined for Western blot were stored in carbogen-gassed aCSF at RT, and pretreated with control medium for 3 hr, control medium (1 hr) and then 40 pM - 1 nM MTX (2 hr) or 5 µM calpeptin (1 hr) + MTX (2 hr). Slices were then homogenized and lysed with a buffer containing (mM): 150 NaCl, 50 Tris, 2.5 $CaCl_2$, 2.5 EGTA, 1% NP-40, pH 7.5, phosphatase inhibitor (P5726, Sigma-Aldrich) and proteinase inhibitor (04693124001, Roche). Lysates were mixed with the 4x Laemmli sample buffer (Bio-Rad, Cat#

1610747) and boiled at 95°C for 5 - 10 min before being resolved with 10% SDS-PAGE gel. Proteins were transferred to a 0.2 µm PVDF membrane (Millipore) and probed with primary antibodies to spectrin αII (Abcam, ab11755) or spectrin βIIC (Abcam, ab264177) overnight at 4°C, followed by HRP-conjugated secondary antibodies (***Supplementary Table S5***). Blot images were taken with a ChemiDoc imager and band densities were analysed with Image Lab (Bio-Rad).

Electrophysiology: Slices were transferred to a recording chamber and recorded at 32°C on the stage of an Olympus BX51W1 scope. Whole-cell patch recordings were obtained using a Multiclamp 700B amplifier, Digidata 1440A to digitize at 40 kHz and analysed with pClamp 10.5 software. Glass pipettes of 1.5 mm O.D. (A-M Systems) and 4-8 MΩ resistance were prepared using a P-95 puller (Sutter Instruments). For voltage clamp recordings, series resistance was compensated to at least 70% and cells with a leak current > 100 pA at the holding potential of -70 mV were rejected for subsequent recordings. To record the IsAHP we used established protocols (King *et al*, 2015; Sahu *et al*, 2017) with steady state commands from -100 mV to +40 mV for 200 ms before stepping back to -50 mV. To isolate the IK-mediated component of the sAHP the bath solution included picrotoxin (50 µM), TTX (1 µM), DNQX (10 µM), DL-AP5 (25 µM), XE-991 (10 µM), apamin (100 nM), TEA (2.5 mM), 4-AP (2.5 mM), and CsCl (2 mM). The internal solution contained (mM): 130 $KMeSO_4$, 0.1 EGTA, 10 HEPES, 7 NaCl, 0.3 $MgCl_2$, and 2 ATP, 0.5 GTP, 5 phosphocreatine were added from frozen stock each day, pH 7.3 adjusted with KOH. Together these solutions established an E_{Cl} of -76 mV and E_K of -97 mV.

Immunocytochemistry

Cultured cells: At 10-15 days *in vitro* (DIV) coverslips with cells were washed with phosphate-buffered saline (PBS) and fixed in 4% paraformaldehyde (PARA) (Electron Microscopy Sciences, ON) in PBS for 10-15 min. After 3 washes in PBS cells were incubated with a blocking medium consisting of (5% (w/v) bovine serum albumin (Vector Laboratories) and 0.2% (v/v) Triton X-100 (Sigma Aldrich) in PBS for 45 min at RT (~22°C) for all subsequent treatments (***Supplementary Table S5***). Cells were incubated with primary antibodies in a blocking medium for 45 min at RT. After five 10 min washes in blocking medium cells were treated with the secondary antibodies for 45 min at RT. After three rounds of 10 min washes in blocking solution cells were washed once in PBS and post-fixed with 4% PARA and 0.1% glutaraldehyde in PBS for 10 min followed by three 10 min washes in PBS. TetraSpek™ beads (1:2000, 100 nm diameter, T7279, Thermofisher) were added to coverslips overnight at 4ºC in PBS followed by three 5 min washes in PBS to remove loose beads.

Freshly fixed intact hippocampus: Free floating coronal sections were prepared from P21-26 rats following isoflurane anesthesia until unresponsive to tail pinch. Brains were fixed by transcardiac perfusion of saline and subsequently fresh 4% PARA (pH 7.4), and after dissection in 4% PARA at RT for 1 hr and then at 4°C overnight. Free floating coronal sections of 50 µm thickness were cut by vibratome (Leica VT1000S) and treated with a blocking buffer consisting of 3% (v/v) donkey serum and 3% (v/v) goat serum (Jackson ImmunoResearch), 2% (v/v) dimethyl sulfoxide (BDH) and 0.1% (v/v) Tween 20 (Sigma Aldrich) in PBS for 45 min at RT. Primary antibodies were applied in blocking medium overnight at 4°C and STED compatible secondary antibodies applied for 2 hr at RT (***Supplementary Table S5***), separated by 3 X 10 min washes in blocking medium throughout. Tissue sections were finally washed in PBS and coverslipped in ProLong Gold antifade (Invitrogen P36934) for imaging 24-48 hr later.

Live Hippocampal tissue slices: Hippocampal sections of 200 µm thickness were prepared as described

above (*In vitro* tissue slices). After recovery, live hippocampal slices were maintained in carbogen-bubbled aCSF and pretreated with DMSO (control) or 5 μM calpeptin for 1 hr before addition of 40 pM - 1 nM MTX. Sections were then removed and fixed (4% PARA) for 2 hr RT before washing and incubated in blocking medium (as above) for reaction with primary antibodies overnight. Sections were then washed in blocking medium and treated with secondary antibodies (2 hr RT) before washing in PBS, mounting and coverslipped in ProLong Gold antifade (Invitrogen P36934) for imaging 24-48 hr later (***Supplementary Table S5***).

Direct Stochastic Optical Reconstruction Microscopy (dSTORM)

dSTORM imaging was used together with TIRF illumination to localize CaRyK complex proteins within 150 nm of the coverslip surface of MAP-2 positive cultured neurons. Imaging cocktail was prepared fresh from 1X PBS, 10% (w/v) glucose, 10 mM β-mercaptoethanol in an oxygen-scavenging GLOX solution containing 0.5 mg/ml glucose oxidase and 40 μg/ml catalase (Sigma-Aldrich). 10X GLOX solution was prepared as a stock and stored in aliquots at −20°C. On the day of imaging an aliquot of GLOX solution was used to prepare the dSTORM imaging buffer. Imaging cocktail was placed into a concavity slide, covered with the immunolabeled 18 mm coverslip and sealed with VALAP (equal parts vaseline, lanolin and paraffin). Images were obtained using a Quorum Diskovery Flex microscope equipped for TIRF illumination (150 nm depth) using a HC Plan Apo 63X/NA 1.47 oil immersion objective and Andor iXon Ultra 897 EMCCD camera. Fluorophores were first photo switched into a temporary dark state using strong intensity laser illumination (laser power: 561 nm, 55 mW @ 100%; 647 nm, 53 mW @ 100%). Subsets of active blinking fluorophores were then imaged at a lower laser intensity (70-95% excitation) using a 33 Hz frame rate. The 405 nm laser line was adjusted to obtain a balanced reactivation of Alexa Fluor-647 or Cy-3 dyes during image acquisition of 5000-8000 frames per sample.

Image reconstruction was carried out as previously described (Sahu *et al*, 2019) using a ThunderSTORM plugin (Fiji, ImageJ). A calibration factor of 150.5 nm / pixel was obtained under our imaging conditions after rigorous calibration using a slide mounted Supracon nanoscale standard linewidth/pitch target (Part number Kali2020_2_F5; Supracon, Germany) (Live Cell Imaging Facility, University of Calgary). The acquired images were filtered using the wavelet filter function of ThunderSTORM with default values (beta spline order of 3 and a scale of 2), for determining signal-to-noise threshold for the datasets. The camera parameters used were pixel size: 150.5 nm; photoelectrons per A/D count: 8.98; base level A/D count: 200; EM gain: 300. Afterward, the point spread function of the imaged fluorophore localizations were detected with the standard gaussian filter method and fitted with a weighted least square fitting using the subpixel localization fitting procedure of ThunderSTORM. Only the localizations falling under a standard deviation of the fitting distance, representing sigma >50 and <500 were taken into further analysis. Any mechanical drift over the timeframe required for imaging over 15-20 min (0 to <500 nm) was drift corrected using the cross correlation function of ThunderSTORM, with any cases approaching 700 nm excluded from analysis. Correct image reconstruction and alignment for dual labeled images were assured using the X-Y coordinates of 3-6 100 nm fiducial beads (T7279, Thermofisher) as reference points to align signals with an affine/linear registration function using Localization Microscopy Analyzer (LAMA) (Malkusch & Heilemann, 2016). X and Y positional coordinates and intensity information of point localizations were analyzed using the morphological cluster analysis pipeline of LAMA software to identify the coordinates of protein clusters with a minimum cluster radius of 25 nm.

Image Analysis

Extensive work on the pattern of actin and spectrin labeling in axons and dendrites has defined a structural entity referred to as a Membrane Periodic Structure (MPS) (Han *et al*, 2017; Xu *et al*, 2013; Zhong *et al*, 2014; D'Este *et al*, 2015; Unsain *et al*, 2018; Zhou *et al*, 2022; Lorenzo *et al*, 2023). Obtaining a measure of the periodicity of proteins along the MPS was obtained using autocorrelation on ROIs that defined the linear projection of given axons or dendrites. The issue is more complicated in somatic regions where even closely spaced immunolabel clusters could project in any x-y coordinate. For this reason both NND and NMF were used to systematically search through pixels in an ROI that included the lateral borders and entire cytoplasmic region of the soma defined by MAP2-GFP labeling.

STORM analysis of spatial relationships was carried out on either single immunolabels or on centroids reflecting an overlap of fluorophore emissions by calculating the geometric mean (***Fig. S6***). While the extraction of centroids with overlapping pixels served to eliminate single labeled clusters, we note that it also had the effect of underestimating the total number of co-associated clusters that appeared to be in immediate apposition, if only through a function of parallax of vertically aligned proteins. For example, with STORM imaging of cells dual labeled for spectrin βII and Cav1.3, the total number of spectrin βII centroids was 6,741. The process of extracting spectrin βII clusters that overlapped with Cav1.3 clusters reduced the detected spectrin βII centroids by 53% to a total of 3,191. Despite these reductions in centroids detected, NMF analysis typically applied to 8-13 dual labeled cells with 900-5,100 centroids that generated 9-22 features for clusters associated in rows and 14-34 features for isolated clusters. Analysis of the percentage overlap of colabelled CaRyK protein clusters as determined by the portion of pixels with intensity higher than a threshold of 0.2 in both channels is shown in ***Supplementary Table S4***.

Nearest Neighbour Distance (NND)

Intensity information and close proximity of individual fluorophores of the ThunderSTORM/LAMA reconstructions were used to create a mask and identify immunolabeled clusters using the standard morphological cluster analysis (MCA) module of LAMA (Sahu *et al*, 2019; Higham *et al*, 2019; Malkusch & Heilemann, 2016). Cluster centroid information obtained from MCA analysis was used to determine nearest neighbour Euclidean distances in MATLAB (Sahu *et al*, 2019; Higham *et al*, 2019). Distributions were computed for each immunolabel cluster set (eg. Cav1.3-Cav1.3, Cav1.3-RyR2) and fit with either a single gamma distribution or a gamma mixture model using the MATLAB function *lsqnonlin* to define central tendency of the sub-populations in the distributions (Vegas-Sánchez-Ferrero *et al*, 2014). Mixing portions are the integral of each gamma distribution in comparison to the integral of the gamma-mixture model. To assess the spatial randomness of clusters, the NND distributions were further compared to that of the same number of centroids with randomized positions and histograms assessed with the Kosmolgov-Smirnov test in MATLAB (***Fig. S1***).

Non-negative matrix factorization (NMF)

NMF is a computational algebraic tool for reducing dimensionality in data (Berry *et al*, 2007). As a form of singular value decomposition, NMF generates two matrices reflecting a collection of 'features' and weights', of which the product approximates the input data. A strength of NMF is its capacity to define patterns within a dataset when data has been standardized. Ultimately NMF provides a means to compress hundreds of standardized images and reduce them into a handful of 'feature' images (for reviews see (Wang & Zhang, 2013; Berry *et al*, 2007)).

A brief summary of the process for NMF analysis used here is presented in ***Fig. S2-S5*** for the case of spectrin βIIC imaged by STORM-TIRF in neural processes external to the soma, with parameters used for extracting features from somatic labels applied to these images. First, STORM-TIRF images confirmed that the resolution of our system was sufficient to identify the repeating domains of spectrin βII in both MAP2 negative (presumed axons) and MAP2 positive (presumed dendrites) of cultured neurons consistent with an MPS structure. Images were prepared for NMF analysis using a MATLAB script which normalized image intensities and identified centroids through image segmentation using the *regionprops* function. To standardize pattern detection for clusters initially oriented in any x-y direction, ROIs centered around every centroid position were stored as 2D 600-X-600 pixel (4.5 X 4.5 µm) images and rotated so the nearest centroid was oriented to the left (***Fig. S2***). The MATLAB function *nnmf,* from the 'machine learning toolbox', with the default alternating least squares algorithm, and random initialization matrices was used.

Images at the soma identified two broad classes of cluster organization identified by NND analyses: one with closely repeating peaks and another with few peaks and greater spatial separation. Long segments of repeating spectrin clusters were particularly evident in neural processes even though isolated clusters were also detected (***Fig. S2D-G***). NND analysis in neural processes confirmed a high proportion of clusters separated with a periodicity of 144 nm, as well as a smaller population of longer inter cluster distances (***Fig. S2D***). Since these patterns at the soma were typically contained within a distance of 1200 nm on NND distributions and ~150 subpixels on 1D cluster intensity profiles of aligned images, feature categorization of spectrin βII by NMF in neural processes was restricted to a window of -150 to 100 subpixels (-1128 nm to 752 nm).

NMF was employed to derive 6 features from the collection of 118 to >2000 (668 ± 25) centroid images stored from each image channel per cell (Berry *et al*, 2007). Extending the number of features beyond 6 resulted in instances where the centering centroid required as a reference point from which inter-cluster distances were measured, was diminished or absent in features (***Fig. S3A***). Extracting 6 feature sets from the data reduced this deviation from the true images while still maximizing the number of features to process and the quality of the approximations (***Fig. S3, B and C***). Examples of 6 features extracted from spectrin βIIC labeled neural processes external to the soma of a single cell are shown in ***Fig. S3D***. After smoothing with *spaps*, peaks in the 1D feature data were detected using the *findpeaks* function with a minimum distance, prominence, and height threshold of 12, 0.1% of max, and 5% of max, respectively. 1D features were then classified as regularly spaced clusters (rows) (***Fig. S2F***) when 4 or more peaks were found in the detection window, or isolated clusters when 2 or 3 peaks were located (***Fig. S2G***). Features with less than 2 peaks were discarded.

Comparison of NMF to autocorrelation

To fully validate the use of NMF, we tested its ability to quantify the MPS pattern of spectrin βIIC labeling in neuronal processes compared to conventional autocorrelation (***Fig. S4***). STORM-TIRF images of spectrin in MAP2-positive or MAP2-negative processes outside of the soma provided well defined rows of closely spaced clusters for spectrin βII (***Fig. S4, A and B***). Autocorrelation was applied to 28 of each of these classes of spectrin βII labeled clusters outside of the soma to derive a period of 152 ± 2.38 nm (n = 7) for MAP2 negative processes (***Fig. S4C***). Application of NMF to MAP2 negative processes calculated a period of 148 nm ($R^2 = 0.9$) (***Fig. S4D***). While the period derived by autocorrelation and NMF are statistically different (p = 0.010, t-stat = 2.6393) the mean values differed by less than 3%. In comparing the results for MAP2 positive datasets, autocorrelation returned a period of 156 ± 4.34 nm

and NMF a period of 157 nm ($R^2 = 0.84$), results that were not significantly different ($p = 0.752$, t-stat = 0.3234) (***Fig. S4, C and D***).

Fitting of row periods and isolated cluster distances

On the basis of these forms of analyses we applied NMF to extract features to define the periods of regularly spaced clusters by fitting inter-peak distances with a damped oscillatory model (**Eq. 1**) using *lsqnonlin* in MATLAB (***Fig. S5, A and B***). Fitting this model along the entire data range yielded interpretable results but was optimized to the range of 112-526 nm. The lower limit of this was chosen just within a limit set by the peak detector (90 nm). The higher limit was to ensure the models were fit to the highest signal-to-noise region of the data, and match the most common row length (3 clusters) observed in the soma.

$$\textbf{Eq. 1}\quad f(x) = Ae^{(-\alpha x)}\cos\left(\frac{2\pi}{T}(x + \Phi)\right) + ye^{(-vx)}$$

Equation 1 variables: A = amplitude; α = amplitude decay; T = period; Φ = horizontal phase shift; y = baseline; v = baseline decay

Optimal fitting was performed on raw and smoothed data (***Fig. S5, A and B***) using preset and user specified initial values for the least squares solver. This raw and smooth data was amplitude normalized prior to initial value selection to make user values more predictable (***Fig. S5B***), but rescaled to the original data after fitting. Four iterative fits were performed using each initial value set with increasing freedom in the parameters (***Fig. S5B***). The parameters that generated the smallest SSQ in the third or fourth fit were used to define the oscillatory model reported.

Isolated features were examined in a window of -376 to -1506 nm (***Fig. S5F***) from the centering cluster to ensure analysis avoided interpretation of very distant clusters and that gaussian fitting was not disrupted by the tails of the centering centroid. Single gaussian fits were applied to data in the examination window using the function *fit*. These gaussian models were used as proxies of the peak data as isolated point-spread-functions are expected to have a gaussian distribution. The standard deviation and mean of these fitted gaussians were plotted on two axes to identify the number of populations in each data set (***Fig. S5G***). Outliers in either standard deviation or mean of the gaussian fit were identified and culled using the function *rmoutliers* in MATLAB (***Fig. S5G***). Remaining gaussian distributions with means outside of the initial examination window (-376 to -1506 nm) or an excessive standard deviation (SD >= 400) were removed. Finally gaussians with a poor goodness of fit ($R^2 \leq 0.9$) were excluded. The remaining mean positions were plotted as a histogram (***Fig. S5H***) and fit with a single gamma distribution with the median reported. The quality of these gamma distributions and their means were assessed by comparing the gamma model median (the median of the means) to the data median along with R^2.

Row length and branch angles

To determine row lengths and row branch angles visual counting was performed at high resolution by two viewers. After defining all relevant centroids in the image, a random sample of 5 centroid ROIs per cell were selected with the condition of ROI centers being 600 subpixels apart to prevent double counting. These ROIs were overlaid with detected centroid markers and counted for the length of linear rows with a minimum of 3 clusters drawn from 13-55 cells per label. Up to 388 rows for CaRyK complex proteins, actinin I and II, and spectrin βII were defined across a selection of up to 275 ROIs and 55 cells

(**Fig. 2**). A hand selected subset of the randomly picked centroid ROIs was then brightened and used to measure angles when rows of at least 3 consecutive clusters reached a point where a second row of clusters extended with a shift in orientation. Approximately 100 branch points were measured by two viewers for each label across 22-52 ROIs randomly selected from 13-18 cells. Angle measures were generated using Fiji ImageJ.

Stimulated Emission Depletion Microscopy (STED)

STED micrographs were obtained using a STEDYcon (Abberior, Germany) mounted on an Eclipse Ti microscope frame (Nikon, Japan). All images were captured with a Plan APO λD 100X/1.45 NA oil immersion lens (MRD71970, Nikon). STED settings were as follows: excitation laser 2.5% (640 nm laser) or 25.5% (561 nm laser), a depletion laser with a size of ~60 nm (42.0%/74.5% power 775 nm laser), 4 line accumulations, pixel dwell of 10 µs, gate 1-7 ns, and a pinhole set to 64 µm. Z-stacks were taken for every image with a pixel size of 30 x 30 x 250 nm (X, Y, Z) using a piezoconcept stage controlled with a TTL pulse (Piezoconcept, France). STED micrographs were deconvolved using Huygens Professional (v25.04.0p2 64b, Scientific Volume Imaging, The Netherlands)

For STED imaging in tissue sections a complex tissue architecture and cell curvature reduced the area of cell surface per focal plane compared to STORM-TIRF, and thus fewer clusters per cell to apply NMF. A lower resolution in the z axis for 2D STED (~1400 nm) compared to STORM-TIRF (~150 nm) also increased the potential to include immunolabeled clusters below the membrane surface that could affect NMF. Therefore we focused on NND to assess the extent of colocalization of dual labels. Z-stacks were defined using a line scan intensity profile along the z-axis together with MAP2 labeling as a cytoplasmic marker to help define channel labels positioned at the membrane. Plasma membrane-containing optical sections were identified near the top of image stacks that spanned from the nucleus through to the cell exterior, with lateral cell boundaries identified from the deeper cross section images. Centroid and NND determinations were slightly modified from the STORM workflow. Briefly, overlap regions in STED were defined using an 'AND' operator on binary masks from the two channels. Watershed and weighted centers were then determined for each area using the geometric mean overlap image as reference. With centroids determined, fitting and comparisons were performed as described in the STORM analysis.

Source Data

All 1D NMF outputs, NND results, fitting results, and representative raw image files have been deposited at the Federated Research Data Repository and are publicly available. Accession numbers and the DOI are located in ***Supplementary Table S5***. Any further data can be requested from the corresponding author. Original MATLAB and R scripts have been deposited at the Federated Research Data Repository, and are publicly available as of the date of publication.

Statistical Analysis

For STORM-TIRF images, NND and NMF calculations were applied to typically >500 clusters per label/cell (675 ± 26; n = 279) and up to 43,000 clusters in up to 55 cells per label. NND calculations for STED spectrin αII images consisted of >100 clusters per cell (350 ± 25; n = 37) and for IK > 70 clusters per cell (229 ± 19; n = 37).

Smoothing of 1D peak intensity data was done using the spline function *spaps* in MATLAB. Smoothing of raw interpeak data was performed using a moving average *smooth* with its default span of 5 in

MATLAB. Interpolation of fitted gamma distributions was utilized to calculate central tendency with higher precision than the bin width of the histogram data. Fitting was performed using two methods. NND distributions and isolated peak positions were fitted with a single or dual gamma distribution using the function *lsqnonlin* in MATLAB. All single distribution fits had their model median compared to the data median to determine general error in this method. Error decreased and R^2 increased as θ increased. Interpeak distances from row features were fitted with a damped oscillatory model (Eq 1) iteratively using *lsqnonlin* in MATLAB. Goodness of fit was determined with *gfit2* or internally in functions such as *fit.* To determine if distributions were statistically different we utilized the non-parametric Kosmolgov-Smirnov test in MATLAB. To determine if a single value was likely to belong to a distribution a one-sample t-test was used. Comparisons of two normally distributed datasets were determined with two-sample t-tests or Welch's t-test. Comparisons of centroid counts per image, Mander's correlation coefficients and overlap coefficients were performed with a Wilcoxon ranksum test *ranksum* in MATLAB.

Figure Legends

Figure 1. IK and Cav1.3 immunolabels exhibit a coordinated pattern of expression in hippocampal neuronal somata.

(**A**-**B**) STORM-TIRF images of immunolabeled clusters for the indicated proteins detected within 150 nm of the membrane surface. A larger field of view (**A**) and magnified ROIs (**B**) reveal a punctate and organized pattern, with IK or Cav1.3 clusters distinguished as rows of clusters on which the alternate label is closely associated or overlaps at discrete intervals (**B,** ROI-1-4, *solid arrows*). Rows of clusters can reach branch points from which one or two rows of clusters extend (**B,** ROI-4, 6, *open arrows*). In other cases IK or Cav1.3 clusters are present in isolation or in close association with the alternate immunolabel **(B,** ROI-5, 7). **(C-E)** NND analysis between clusters in dual labeled cells reveals two populations between similar labels (**C-D**) and a right skewed single peak for IK-Cav1.3 (**E**). (**F-K**) NMF analysis of dual immunolabels that exhibit fluorescence overlap defines a periodic pattern for cluster rows identified by a damped oscillatory model (**F-H**) or isolated clusters (**I-K**). Unless otherwise indicated, in this and all other figures values for fits (**C-E, I-K**) represent the median of gamma distributions. R^2 values are for the sum of gamma fit distributions (**C-E**), and model periods with R^2 values (**F-H**). Sample values (n) = cells, θ = features. Scale bars: (**A**) 5 µm; (**B**, ROI-1, -2), 1 µm; (**B,** ROI-6), 500 nm; (**B**, ROI-3, 4, 5, and 7), 250 nm. Bin width: (**C-E**) 25 nm, (**F-H**) 15 nm, (**I-K**) 20 nm. See also ***Fig. S1*; *Supplemental Tables S1 and S2***.

Figure 2. Correspondence between the spatial organization of CaRyK complex protein clusters and cytoskeletal elements. Plots of the percent of immunolabeled clusters aligned in rows of at least three clusters, and histogram plots of the angles at branch points of cluster rows for CaRyK complex proteins (**A, B**) and cytoskeletal elements (**C, D**). Images were examined at high resolution in up to 5 randomly selected ROIs of 600 X 600 pixels / cell drawn from 9-55 cells per label. For both CaRyK complex proteins and cytoskeletal elements, 40-60% of all clusters are contained within rows of 3, with a decrease to ~20-25% of clusters in rows of 4, and to only a few percent in rows of up to 8 clusters. Bin widths: 5 degrees. Mean and S.E.M. of angles are shown, with no statistical difference found between any of the distributions of angles for branch points of rows of CaRyK proteins, actinin I or II, or spectrin βII (see also Materials and Methods, and ***Supplemental Table S3***).

Figure 3. RyR2 exhibits a regular pattern of expression in relation to Cav1.3 and IK. (**A-D**) STORM-TIRF images of immunolabeled clusters for the indicated proteins. Larger field views (**A-C**) and magnified ROIs (**B-D**) show that RyR2 clusters exhibit an organized pattern in relation to Cav1.3 (**A-B**) or IK (**C-D**). RyR2 clusters are distributed in rows (**B,** ROI-1, *arrowheads*) that can reach branch points (**B-D,** *open arrows*) or be positioned in isolation. Cav1.3 and IK labels share these patterns and colocalize with RyR2 as rows of clusters (**B,** ROI-1, *arrowheads;* **B** and **D,** ROI-2, *filled arrows*) or as isolated labels. (**E-G**) NND analysis of dual labeled cells reveals two populations of distance between RyR2 clusters (**E**) and right-skewed single peaks for RyR2-Cav1.3 (**F**) or RyR2-IK (**G**). (**H-M**) NMF analysis defines a periodic pattern for colabeled cluster rows (**H-J**) or a single distribution for isolated clusters (**K-M**). Sample values (n) = cells, θ = features. Calibration bars: (**A-C**) 5 µm; (**B-D**) 2 µm. Bin widths: (**E-G)** 25 nm, (**H-J**) 15 nm, (**K-M**) 20 nm. See also ***Fig. S1, Supplemental Tables S1 and S2.***

Figure 4. Spectrin βII exhibits a structured pattern associated with Cav1.3. (**A-D**) STORM-TIRF images of immunolabeled clusters for the indicated proteins. Shown are larger fields of view for a cell labeled for spectrin βII (**A** and **B**) and the same cell dual labeled for spectrin βII and Cav1.3 (**C** and **D**). ROIs are magnified in (**B** and **D**), with the same frame of view in (**B,** ROI-2) and (**D,** ROI-1). (**B** and **D**) Spectrin βII labeled clusters organize as rows of clusters (*arrowheads*) that extend to branch points (*open arrows*) or as isolated clusters (*filled arrows*). Dual labeling reveals Cav1.3 clusters that overlap with spectrin βII cluster rows (**C** and **D,** ROI-1, 2, *arrowheads*). (**E-F**) NND in dual labeled cells reveals two populations between spectrin βII clusters (**E**) and one for spectrin βII-Cav1.3 (**F**). (**G-J**) NMF analysis defines a periodic pattern for cluster rows (**G** and **H**) or a single distribution for isolated clusters (**I** and **J**). Sample values (n) = cells, θ = features. R^2 value in (**E**) corresponds to the superimposed combined fit for the two populations. Scale bars: (**A** and **C**) 5 µm; (**B,** ROI-1, -2; **D,** ROI-1), 2 µm; (**D,** ROI-2), 500 nm. Bin widths: (**E-F)** 25 nm, (**G-H**) 15 nm, (**I-J**) 20 nm. See also ***Supplemental Tables S1 and S2.***

Figure 5. Spectrin exhibits an organized pattern that is closely associated with IK and RyR2 distributions. (**A-D**) STORM-TIRF images of immunolabeled clusters for the indicated proteins. Larger field views (**A** and **C**) with ROIs magnified (**B** and **D**) identify rows of spectrin βII clusters that can reach branch points (*open arrows*) that colocalize or alternate with rows of IK or RyR2 (*arrowheads*). Isolated clusters can be distinguished for IK or RyR2 (**B,** ROI-2, **D**, ROI-1, 2; *filled arrows*). (**E-F**) NND analysis between IK-spectrin βII (**E**) and RyR2-spectrin βII (**F**). (**G-J**), NMF analysis defines a periodic pattern for cluster rows (**G-H**) or a single distribution for isolated clusters (**I-J**). Sample values (n) = cells, θ = features. Scale bars: (**A** and **C**) 5 µm; (**B** and **D**, ROI-1, -2), 1 µm. Bin widths: (**E-F)** 25 nm, (**G-H**) 15 nm, (**I-J**) 20 nm. See also ***Fig. S7, Supplemental Table S1 and S2***.

Figure 6. Actinin I and actinin II distributions are aligned with CaRyK complex proteins. (**A-F**) STORM-TIRF images of immunolabeled clusters for the indicated proteins. Shown are dual labeled images for the indicated CaRyK complex proteins and actinin isoforms. Larger field views (**A, C, E**) and associated ROIs (**B, D, F**) identify clusters that align in rows that either overlap or alternate (*arrowheads*) with actinin isoforms. Cluster rows can extend to branch points (*open arrows*), colocalize (*solid arrows*), or alternate to extend or bridge rows of labels (*arrowheads*). (**G-I**) NND analysis between actinin I - Cav1.3 (**G**), actinin II - IK (**H**) and actinin II - RyR2 (**I**). (**J-O**) NMF analysis defines a periodic pattern for cluster rows (**J-L**) or a single distribution for isolated clusters (**M-O**). Sample values (n) = cells, θ = features. Scale bars: (**A, C, E**) 5 µm; (**B, D, F**), 1 µm. Bin widths: (**G-I)** 25 nm, (**J-L**) 15 nm, (**M-O**) 20 nm. See also ***Figs. S8 and S9, Supplemental Tables S1 and S2.***

Figure 7. The sAHP of CA1 pyramidal cells depends on the integrity of the spectrin cytoskeleton. (**A**) Western blot analysis for spectrin αII in rat P21-26 hippocampal slices pretreated with control aCSF or 5 µM calpeptin for 3 hr, control aCSF (1 hr) and then 1 nM MTX (2 hr), or 5 µM calpeptin (Clpt, 1 hr) + MTX (2 hr). MTX induces breakdown products of spectrin αII at ~150 kDa that are reduced by calpeptin. Mean band densities on Western blots are normalized to the levels of α-tubulin (n = 4). (**B**) Control

NND plots for the whole population of clusters imaged in CA1 pyramidal cell somata of P20-25 rats returns a right skewed histogram (left), and for colocalized clusters (overlapping pixels) a dual exponential fit with median values that is equivalent to that of cultured cells (right). MTX treatment (80 pM, 1 hr) increases the median NND value at the population level and substantially alters the number (***ρ***) and median values of fits for distance between colocalized cluster centers, with values restored by pretreatment with calpeptin. (**C**) Mean bar plots of NND median values for data in (**B**) for the whole population or colocalized data sets under the indicated conditions. Comparison with Wilcoxon ranksum test. (**D**) Whole cell recordings of the IK-mediated IsAHP in CA1 pyramidal cells of P21-P26 rats. IsAHP was evoked by a step command from -100 mV to +40 mV (200 msec) and back to -50 mV. Currents are from cells recorded from control sections, after 1 hr 40 pM MTX, or when exposed to 5 µM calpeptin with or without 40 pM MTX. Mean bar plots of IsAHP amplitude are shown for the indicated conditions. Average values are mean ± S.E.M, Student's *t*-test; * $p < 0.05$; ** $p < 0.01$; N.S., not significant. Sample numbers are shown in brackets. ρ, number of centroids detected across all images for a given label set; ρ/n, mean centroids per cell; R^2 coefficient of determination for combined fit of two populations in (**B**). Bin width (**B**), 30 nm. See also ***Fig. S10 and Supplemental Table S1***.

References

Andrade R, Foehring RC & Tzingounis AV (2012) The calcium-activated slow AHP: cutting through the Gordian knot. *Front Cell Neurosci* 6: 47

Antonucci DE, Lim ST, Vassanelli S & Trimmer JS (2001) Dynamic localization and clustering of dendritic Kv2.1 voltage-dependent potassium channels in developing hippocampal neurons. *Neuroscience* 108: 69–81

Berry MW, Browne M, Langville AN, Pauca VP & Plemmons RJ (2007) Algorithms and applications for approximate nonnegative matrix factorization. *Comput Stat Data Anal* 52: 155–173

Brown JW, Bullitt E, Sriswasdi S, Harper S, Speicher DW & McKnight CJ (2015) The Physiological Molecular Shape of Spectrin: A Compact Supercoil Resembling a Chinese Finger Trap. *PLoS Comput Biol* 11: e1004302

Charlick JN, Bozadzhieva D, Butler AS, Wilkinson KA & Marrion NV (2024) A single coiled-coil domain mutation in hIKCa channel subunits disrupts preferential formation of heteromeric hSK1:hIKCa channels. *Eur J Neurosci* 59: 3–16

Constantin S, Quignon C, Pizano K, Shostak DM & Wray S (2024) Vasoactive intestinal peptide excites GnRH neurons via KCa3.1, a potential player in the slow afterhyperpolarization current. *Front Cell Neurosci* 18: 1354095

Czogalla A & Sikorski AF (2005) Spectrin and calpain: a 'target' and a 'sniper' in the pathology of neuronal cells. *Cell Mol Life Sci* 62: 1913–1924

D'Este E, Kamin D, Balzarotti F & Hell SW (2017) Ultrastructural anatomy of nodes of Ranvier in the peripheral nervous system as revealed by STED microscopy. *Proc Natl Acad Sci U S A* 114: E191–E199

D'Este E, Kamin D, Göttfert F, El-Hady A & Hell SW (2015) STED nanoscopy reveals the ubiquity of subcortical cytoskeleton periodicity in living neurons. *Cell Rep* 10: 1246–1251

D'Este E, Kamin D, Velte C, Göttfert F, Simons M & Hell SW (2016) Subcortical cytoskeleton periodicity throughout the nervous system. *Sci Rep* 6: 22741

Deutsch E, Weigel AV, Akin EJ, Fox P, Hansen G, Haberkorn CJ, Loftus R, Krapf D & Tamkun MM (2012) Kv2.1 cell surface clusters are insertion platforms for ion channel delivery to the plasma membrane. *Mol Biol Cell* 23: 2917–2929

Dixon RE & Trimmer JS (2023) Endoplasmic Reticulum-Plasma Membrane Junctions as Sites of Depolarization-Induced Ca2+ Signaling in Excitable Cells. *Annu Rev Physiol*

Engbers JDT, Anderson D, Asmara H, Rehak R, Mehaffey WH, Hameed S, McKay BE, Kruskic M, Zamponi GW & Turner RW (2012) Intermediate conductance calcium-activated potassium channels modulate summation of parallel fiber input in cerebellar Purkinje cells. *Proc Natl Acad Sci U S A* 109: 2601–2606

Fox PD, Haberkorn CJ, Akin EJ, Seel PJ, Krapf D & Tamkun MM (2015) Induction of stable ER–plasma-membrane junctions by Kv2.1 potassium channels. *J Cell Sci* 128: 2096–2105

Fu J, Dai X, Plummer G, Suzuki K, Bautista A, Githaka JM, Senior L, Jensen M, Greitzer-Antes D, Manning Fox JE, *et al* (2017) Kv2.1 Clustering Contributes to Insulin Exocytosis and Rescues Human β-Cell Dysfunction. *Diabetes* 66: 1890–1900

Gao Y, Perkins EM, Clarkson YL, Tobia S, Lyndon AR, Jackson M & Rothstein JD (2011) β-III spectrin is critical for development of purkinje cell dendritic tree and spine morphogenesis. *J Neurosci* 31: 16581–16590

Glantz SB, Cianci CD, Iyer R, Pradhan D, Wang KKW & Morrow JS (2007) Sequential degradation of alphaII and betaII spectrin by calpain in glutamate or maitotoxin-stimulated cells. *Biochemistry* 46: 502–513

Grum VL, Li D, MacDonald RI & Mondragón A (1999) Structures of two repeats of spectrin suggest models of flexibility. *Cell* 98: 523–535

Gründemann J & Clark BA (2015) Calcium-Activated Potassium Channels at Nodes of Ranvier Secure Axonal Spike Propagation. *Cell Rep* 12: 1715–1722

Hall DD, Dai S, Tseng P-Y, Malik Z, Nguyen M, Matt L, Schnizler K, Shephard A, Mohapatra DP, Tsuruta F, *et al* (2013) Competition between α-actinin and Ca2 -Calmodulin Controls Surface Retention of the L-type Ca2 Channel CaV1.2. *Neuron* 78: 483–497 doi:10.1016/j.neuron.2013.02.032 [PREPRINT]

Han B, Zhou R, Xia C & Zhuang X (2017) Structural organization of the actin-spectrin–based membrane skeleton in dendrites and soma of neurons. *Proc Natl Acad Sci U S A* 114: E6678–E6685

He J, Zhou R, Wu Z, Carrasco MA, Kurshan PT, Farley JE, Simon DJ, Wang G, Han B, Hao J, *et al* (2016) Prevalent presence of periodic actin–spectrin-based membrane skeleton in a broad range of neuronal cell types and animal species. *Proc Natl Acad Sci U S A* 113: 6029–6034

Hiess F, Vallmitjana A, Wang R, Cheng H, ter Keurs HEDJ, Chen J, Hove-Madsen L, Benitez R & Chen SRW (2015) Distribution and Function of Cardiac Ryanodine Receptor Clusters in Live Ventricular Myocytes. *J Biol Chem* 290: 20477–20487

Higham J, Sahu G, Wazen R-M, Colarusso P, Gregorie A, Harvey BSJ, Goudswaard L, Varley G, Sheppard DN, Turner RW, *et al* (2019) Preferred Formation of Heteromeric Channels between Coexpressed SK1 and IKCa Channel Subunits Provides a Unique Pharmacological Profile of Ca2 -Activated Potassium Channels. *Molecular Pharmacology* 96: 115–126 doi:10.1124/mol.118.115634 [PREPRINT]

Huang CY-M, Zhang C, Ho TS-Y, Oses-Prieto J, Burlingame AL, Lalonde J, Noebels JL, Leterrier C & Rasband MN (2017) αII Spectrin Forms a Periodic Cytoskeleton at the Axon Initial Segment and Is Required for Nervous System Function. *J Neurosci* 37: 11311–11322

Johnson B, Leek AN & Tamkun MM (2019) Kv2 channels create endoplasmic reticulum / plasma membrane junctions: a brief history of Kv2 channel subcellular localization. *Channels* 13: 88–101

King B, Rizwan AP, Asmara H, Heath NC, Engbers JD, Dykstra S, Bartoletti TM, Hameed S, Zamponi GW & Turner RW (2015) IKCa channels are a critical determinant of the slow AHP in CA1 pyramidal neurons. *Cell Rep* 11: 175–182

Leterrier C & Pullarkat PA (2022) Mechanical role of the submembrane spectrin scaffold in red blood

cells and neurons. *J Cell Sci* 135

Leung YM, Kang Y, Gao X, Xia F, Xie H, Sheu L, Tsuk S, Lotan I, Tsushima RG & Gaisano HY (2003) Syntaxin 1A binds to the cytoplasmic C terminus of Kv2.1 to regulate channel gating and trafficking. *J Biol Chem* 278: 17532–17538

Liem RKH (2016) Cytoskeletal Integrators: The Spectrin Superfamily. *Cold Spring Harb Perspect Biol* 8

Lim ST, Antonucci DE, Scannevin RH & Trimmer JS (2000) A novel targeting signal for proximal clustering of the Kv2.1 K+ channel in hippocampal neurons. *Neuron* 25: 385–397

Löfvenberg L & Backman L (1999) Calpain-induced proteolysis of beta-spectrins. *FEBS Lett* 443: 89–92

Lorenzo DN, Edwards RJ & Slavutsky AL (2023) Spectrins: molecular organizers and targets of neurological disorders. *Nat Rev Neurosci*

Lukinavičius G, Reymond L, D'Este E, Masharina A, Göttfert F, Ta H, Güther A, Fournier M, Rizzo S, Waldmann H, *et al* (2014) Fluorogenic probes for live-cell imaging of the cytoskeleton. *Nat Methods* 11: 731–733

Lu L, Timofeyev V, Li N, Rafizadeh S, Singapuri A, Harris TR & Chiamvimonvat N (2009) Alpha-actinin2 cytoskeletal protein is required for the functional membrane localization of a Ca2+-activated K+ channel (SK2 channel). *Proc Natl Acad Sci U S A* 106: 18402–18407

Lu L, Zhang Q, Timofeyev V, Zhang Z, Young JN, Shin H-S, Knowlton AA & Chiamvimonvat N (2007) Molecular coupling of a Ca2+-activated K+ channel to L-type Ca2+ channels via alpha-actinin2. *Circ Res* 100: 112–120

Lux SE 4th (2016) Anatomy of the red cell membrane skeleton: unanswered questions. *Blood* 127: 187–199

Machnicka B, Grochowalska R, Bogusławska DM, Sikorski AF & Lecomte MC (2012) Spectrin-based skeleton as an actor in cell signaling. *Cell Mol Life Sci* 69: 191–201

Malkusch S & Heilemann M (2016) Extracting quantitative information from single-molecule super-resolution imaging data with LAMA - LocAlization Microscopy Analyzer. *Sci Rep* 6: 34486

Mandikian D, Bocksteins E, Parajuli LK, Bishop HI, Cerda O, Shigemoto R & Trimmer JS (2014) Cell type-specific spatial and functional coupling between mammalian brain Kv2.1 K+ channels and ryanodine receptors. *J Comp Neurol* 522: 3555–3574

Marek R, Caruso M, Rostami A, Grinspan JB & Das Sarma J (2008) Magnetic cell sorting: a fast and effective method of concurrent isolation of high purity viable astrocytes and microglia from neonatal mouse brain tissue. *J Neurosci Methods* 175: 108–118

Maverick EE & Tamkun MM (2022) High spatial density is associated with non-conducting Kv channels from two families. *Biophys J* 121: 755–768

Moore SJ, Cazares VA, Temme SJ & Murphy GG (2023) Age-related deficits in neuronal physiology and cognitive function are recapitulated in young mice overexpressing the L-type calcium channel, CaV 1.3. *Aging Cell* 22: e13781

Nans A, Mohandas N & Stokes DL (2011) Native ultrastructure of the red cell cytoskeleton by cryo-electron tomography. *Biophys J* 101: 2341–2350

Oblasov I, Bal NV, Shvadchenko AM, Fortygina P, Idzhilova OS, Balaban PM & Nikitin ES (2024) Ca2+-permeable AMPA receptor-dependent silencing of neurons by KCa3.1 channels during epileptiform activity. *Biochem Biophys Res Commun* 733: 150434

Park YS, Sung K-W & Kim I-B (2025) IK channel confers fine-tuning of rod bipolar cell excitation and synaptic transmission in the retina. *Function (Oxf)* 6

Rentsch J, Bandstra S, Sezen B, Sigrist P, Bottanelli F, Schmerl B, Shoichet S, Noé F, Sadeghi M & Ewers H (2024) Sub-membrane actin rings compartmentalize the plasma membrane. *J Cell Biol* 223

Roshchin MV, Ierusalimsky VN, Balaban PM & Nikitin ES (2020) Ca2+-activated KCa3.1 potassium channels contribute to the slow afterhyperpolarization in L5 neocortical pyramidal neurons. *Sci Rep* 10: 14484

Sadeghi A, Doyle AD & Johnson BD (2002) Regulation of the cardiac L-type Ca2+ channel by the actin-binding proteins alpha-actinin and dystrophin. *Am J Physiol Cell Physiol* 282: C1502–11

Sahu G, Asmara H, Zhang FX, Zamponi GW & Turner RW (2017) Activity-Dependent Facilitation of CaV1.3 Calcium Channels Promotes KCa3.1 Activation in Hippocampal Neurons. *J Neurosci* 37: 11255–11270

Sahu G & Turner RW (2021) The molecular basis for the calcium-dependent sAHP in CA1 hippocampal pyramidal cells. *Front Physiol* 1: 1–25

Sahu G, Wazen R-M, Colarusso P, Chen SRW, Zamponi GW & Turner RW (2019) Junctophilin Proteins Tether a Cav1-RyR2-KCa3.1 Tripartite Complex to Regulate Neuronal Excitability. *Cell Reports* 28: 2427–2442.e6

Tiwari MN, Mohan S, Biala Y, Shor O, Benninger F & Yaari Y (2022) Corticotropin Releasing Factor Mediates KCa3.1 Inhibition, Hyperexcitability, and Seizures in Acquired Epilepsy. *J Neurosci* 42: 5843–5859

Tiwari MN, Mohan S, Biala Y & Yaari Y (2018) Differential contributions of Ca2+ -activated K+ channels and Na+ /K+ -ATPases to the generation of the slow afterhyperpolarization in CA1 pyramidal cells. *Hippocampus* 28: 338–357

Tiwari MN, Mohan S, Biala Y & Yaari Y (2019) Protein kinase A-mediated suppression of the slow afterhyperpolarizing KCa3.1 current in temporal lobe epilepsy. *J Neurosci*

Trimmer JS (2015) Subcellular localization of K+ channels in mammalian brain neurons: remarkable precision in the midst of extraordinary complexity. *Neuron* 85: 238–256

Turner M, Anderson DE, Bartels P, Nieves-Cintron M, Coleman AM, Henderson PB, Man KNM, Tseng P-Y, Yarov-Yarovoy V, Bers DM, *et al* (2020) α-Actinin-1 promotes activity of the L-type Ca2+ channel Cav 1.2. *EMBO J* 39: e102622

Turner RW, Asmara H, Engbers JDT, Miclat J, Rizwan AP, Sahu G & Zamponi GW (2016) Assessing the role of IKCa channels in generating the sAHP of CA1 hippocampal pyramidal cells. *Channels* 10: 313–319

Unsain N, Stefani FD & Cáceres A (2018) The Actin/Spectrin Membrane-Associated Periodic Skeleton in Neurons. *Front Synaptic Neurosci* 10: 10

Vegas-Sánchez-Ferrero G, Martín-Fernández M & Sanches JM (2014) A Gamma Mixture Model for IVUS Imaging. In *Multi-Modality Atherosclerosis Imaging and Diagnosis*, Saba L Sanches JM Pedro LM & Suri JS (eds) pp 155–171. New York, NY: Springer New York

Vierra NC, Kirmiz M, van der List D, Santana LF & Trimmer JS (2019) Kv2.1 mediates spatial and functional coupling of L-type calcium channels and ryanodine receptors in mammalian neurons. *Elife* 8

Vierra NC, O'Dwyer SC, Matsumoto C, Santana LF & Trimmer JS (2021) Regulation of neuronal excitation-transcription coupling by Kv2.1-induced clustering of somatic L-type Ca2+ channels at ER-PM junctions. *Proc Natl Acad Sci U S A* 118

Vierra NC & Trimmer JS (2022) Ion Channel Partnerships: Odd and Not-So-Odd Couples Controlling Neuronal Ion Channel Function. *Int J Mol Sci* 23

Wang KK, Nath R, Raser KJ & Hajimohammadreza I (1996) Maitotoxin induces calpain activation in SH-SY5Y neuroblastoma cells and cerebrocortical cultures. *Arch Biochem Biophys* 331: 208–214

Wang K, Mateos-Aparicio P, Honigsperger C, Raghuram V, Wu WW, Ridder MC, Sah P, Maylie J, Storm JF & Adelman JP (2016) IK1 channels do not contribute to the slow afterhyperpolarization in pyramidal neurons. *Elife* 5: e11206

Wang Y-X & Zhang Y-J (2013) Nonnegative Matrix Factorization: A Comprehensive Review. *IEEE Trans Knowl Data Eng* 25: 1336–1353

Xu K, Zhong G & Zhuang X (2013) Actin, spectrin, and associated proteins form a periodic cytoskeletal structure in axons. *Science* 339: 452–456

Zhang Z, Larner SF, Liu MC, Zheng W, Hayes RL & Wang KKW (2009) Multiple alphaII-spectrin breakdown products distinguish calpain and caspase dominated necrotic and apoptotic cell death pathways. *Apoptosis* 14: 1289–1298

Zhong G, He J, Zhou R, Lorenzo D, Babcock HP, Bennett V & Zhuang X (2014) Developmental mechanism of the periodic membrane skeleton in axons. *Elife* 3

Zhou R, Han B, Nowak R, Lu Y, Heller E, Xia C, Chishti AH, Fowler VM & Zhuang X (2022) Proteomic and functional analyses of the periodic membrane skeleton in neurons. *Nat Commun* 13: 3196

Zuccotti A, Clementi S, Reinbothe T, Torrente A, Vandael DH & Pirone A (2011) Structural and functional differences between L-type calcium channels: crucial issues for future selective targeting. *Trends Pharmacol Sci* 32: 366–375

Acknowledgements: We gratefully acknowledge J. Forden for technical assistance, P. Colarusso, C. Brideau, and L. Swift (Live Cell Imaging Facility, Univ. Calgary) for assistance in image calibrations and N.V. Marrion for helpful discussions. This work was supported by the Canadian Institute of Health Research Project Grants MOP136826, PJT 169007 (R.W.T.), Indian Council of Medical Research (ICMR) (IIRP-2023-0253; FIW-2024-01-0000000061; IIRPSG-2025-01-01202) (G.S.), and the Department of

Biotechnology (BT/PR47597/BMS/85/46/2024) (G.S.). W.N. holds a Canada Research Chair in Computational Neuroscience

Author contributions: Authorship: G.S. and D.G. contributed equally to the work; Conceptualization: R.W.T., G.S., W.N.; Methodology: G.S, W.N., D.G., X.Z.; Investigation: G.S., D.G., X.Z., W.N.; Validation: G.S., D.G., W.N., X.Z., R.W.T.; Data analysis: G.S., D.G., W.N., X.Z.; Visualization: G.S., D.G., R.W.T., W.N.; Resources: Live Cell Imaging Facility, University of Calgary; Supervision: R.W.T., W.N.; Funding acquisition: R.W.T., G.S.; Writing, review and editing: All authors wrote or reviewed the manuscript before submission.

Competing interests: The authors declare no competing interests.

Data and materials availability: All the image data and scripts have been deposited to FRDR https://doi.org/10.20383/103.01618

Graphical Abstract:

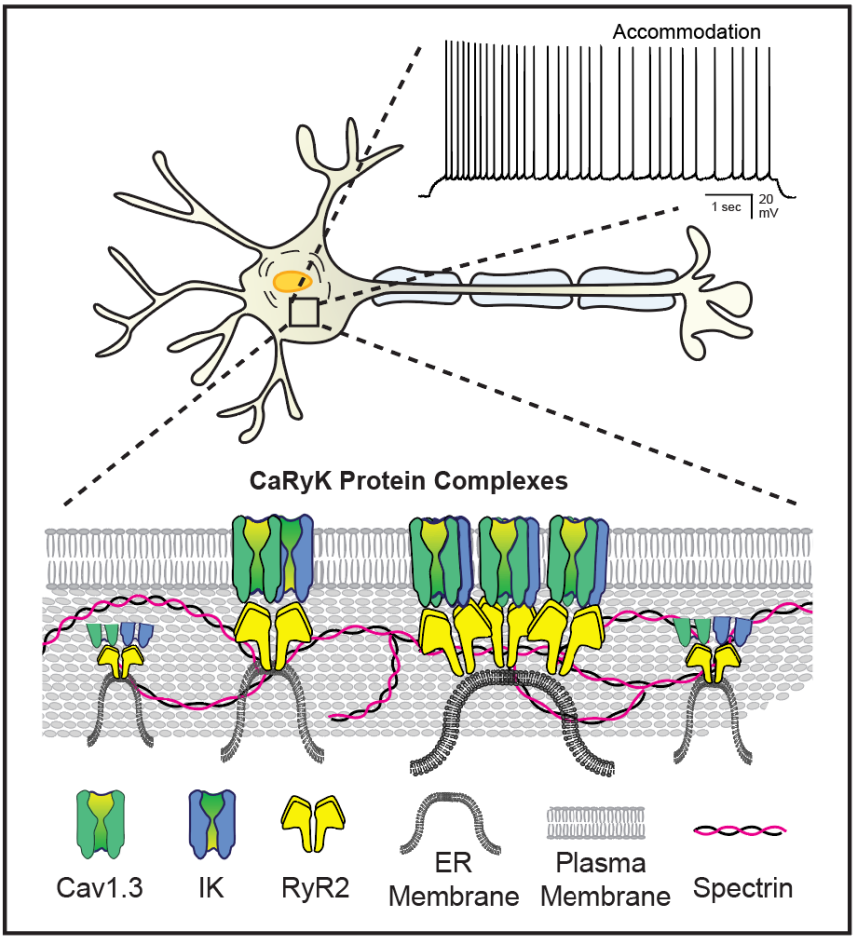

A spectrin-based polygonal framework at the soma coordinates the spatial expression of calcium and potassium channels that drive a slow AHP to regulate spike output. Schematic of a neuron and distribution of CaRyK complex proteins at ER-PM junctions across a matrix of spectrin as cluster rows or as isolated clusters, which together enable an sAHP and spike accommodation in CA1 pyramidal cells.

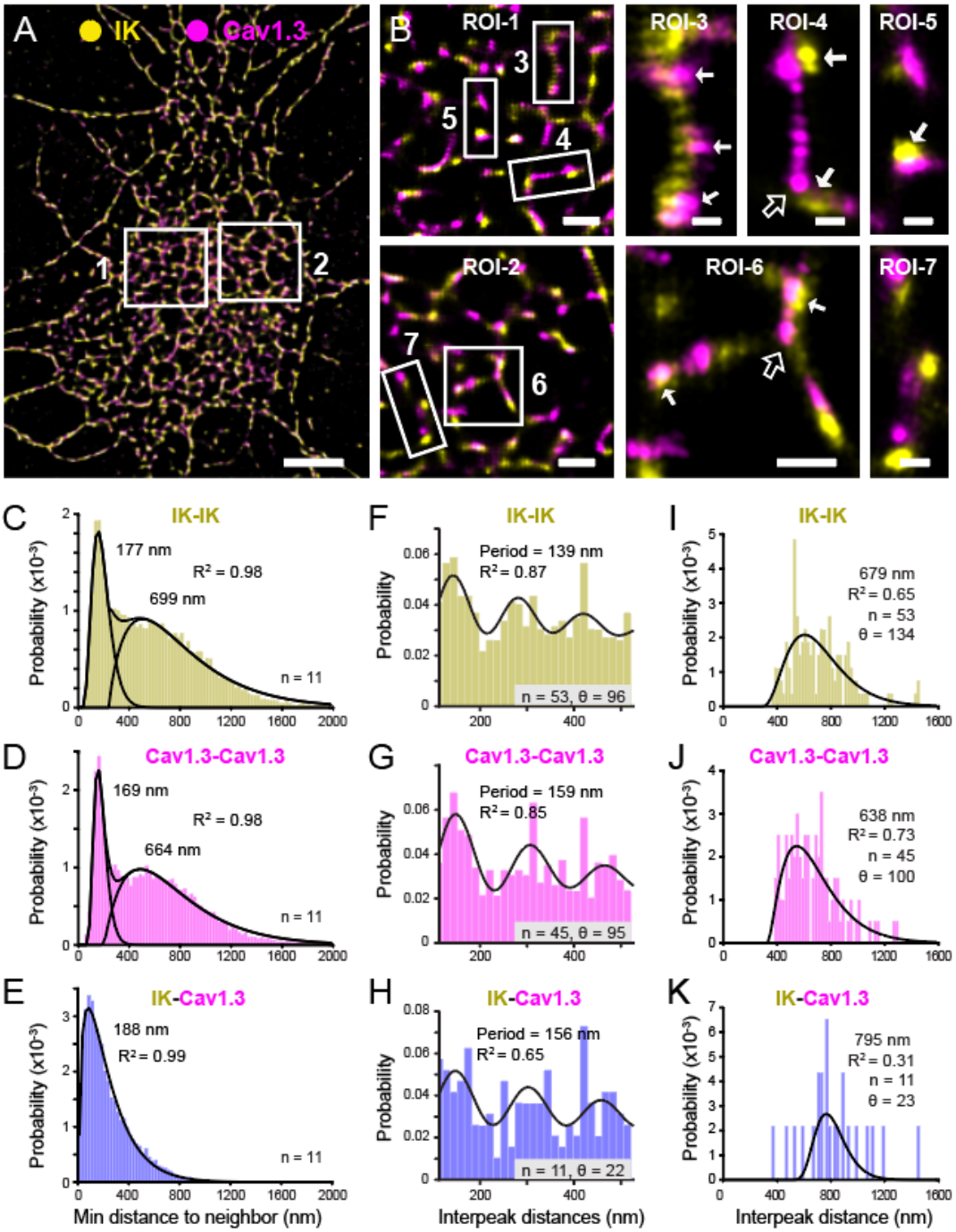

Figure 1. IK and Cav1.3 immunolabels exhibit a co-ordinated pattern of expression in hippocampal neuronal somata.

(**A-B**) STORM-TIRF images of immunolabeled clusters for the indicated proteins detected within 150 nm of the membrane surface. A larger field of view (**A**) and magnified ROIs (**B**) reveal a punctate and organized pattern, with IK or Cav1.3 clusters distinguished as rows of clusters on which the alternate label is closely associated or overlaps at discrete intervals (**B,** ROI-1-4, *solid arrows*). Rows of clusters can reach branch points from which one or two rows of clusters extend (**B,** ROI-4, 6, *open arrows*). In other cases IK or Cav1.3 clusters are present in isolation or in close association with the alternate immunolabel (**B,** ROI-5, 7). (**C-E**) NND analysis between clusters in dual labeled cells reveals two populations between similar labels (**C-D**) and a right skewed single peak for IK-Cav1.3 (**E**). (**F-K**) NMF analysis of dual immunolabels that exhibit fluorescence overlap defines a periodic pattern for cluster rows identified by a damped oscillatory model (**F-H**) or isolated clusters (**I-K**). Unless otherwise indicated, in this and all other figures values for fits (**C-E, I-K**) represent the median of gamma distributions. R^2 values are for the sum of gamma fit distributions (**C-E**), and model periods with R^2 values (**F-H**). Sample values (n) = cells, θ = features. Scale bars: (**A**) 5 µm; (**B**, ROI-1, -2), 1 µm; (**B,** ROI-6), 500 nm; (**B**, ROI-3, 4, 5, and 7), 250 nm. Bin width: (**C-E**) 25 nm, (**F-H**) 15 nm, (**I-K**) 20 nm. See also ***Fig. S1*; *Supplemental Tables S1 and S2***.

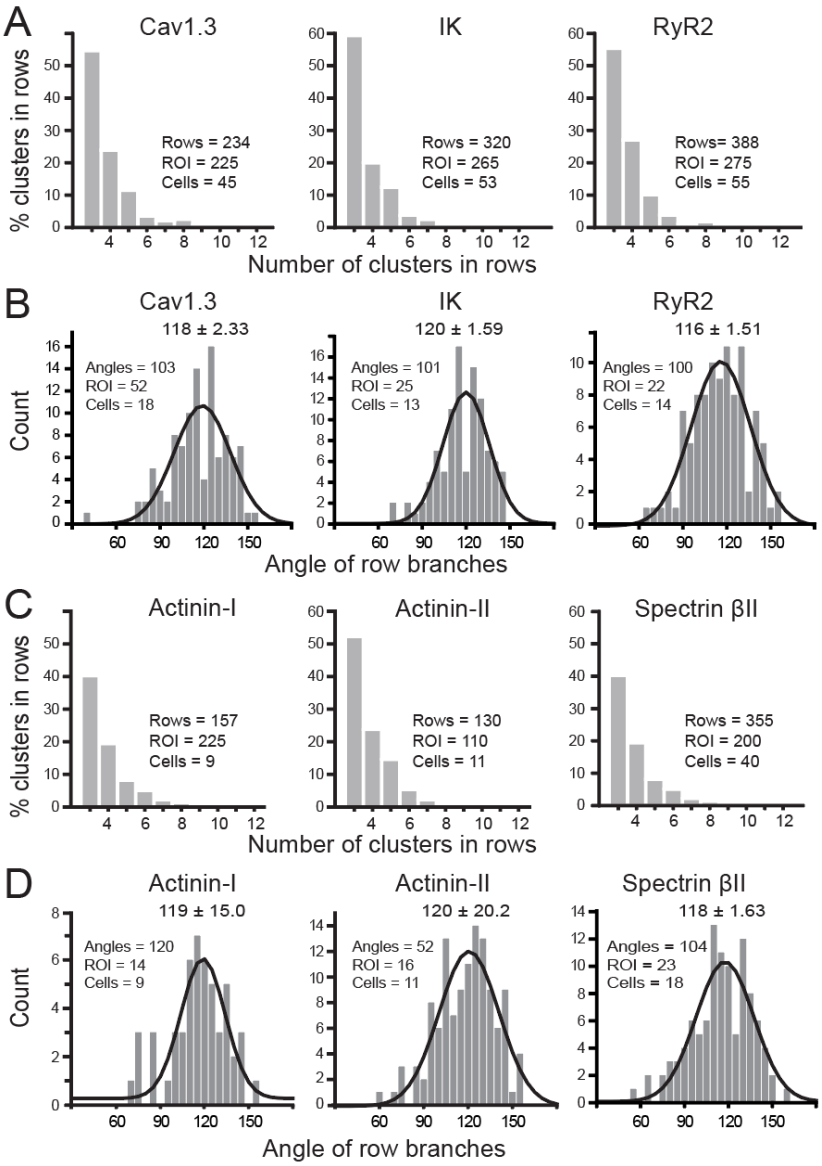

Figure 2. Correspondence between the spatial organization of CaRyK complex protein clusters and cytoskeletal elements. Plots of the percent of immunolabeled clusters aligned in rows of at least three clusters, and histogram plots of the angles at branch points of cluster rows for CaRyK complex proteins (**A, B**) and cytoskeletal elements (**C, D**). Images were examined at high resolution in up to 5 randomly selected ROIs of 600 X 600 pixels / cell drawn from 9-55 cells per label. For both CaRyK complex proteins and cytoskeletal elements, 40-60% of all clusters are contained within rows of 3, with a decrease to ~20-25% of clusters in rows of 4, and to only a few percent in rows of up to 8 clusters. Bin widths: 5 degrees. Mean and S.E.M. of angles are shown, with no statistical difference found between any of the distributions of angles for branch points of rows of CaRyK proteins, actinin I or II, or spectrin βII (see also Materials and Methods, and ***Supplemental Table S3***).

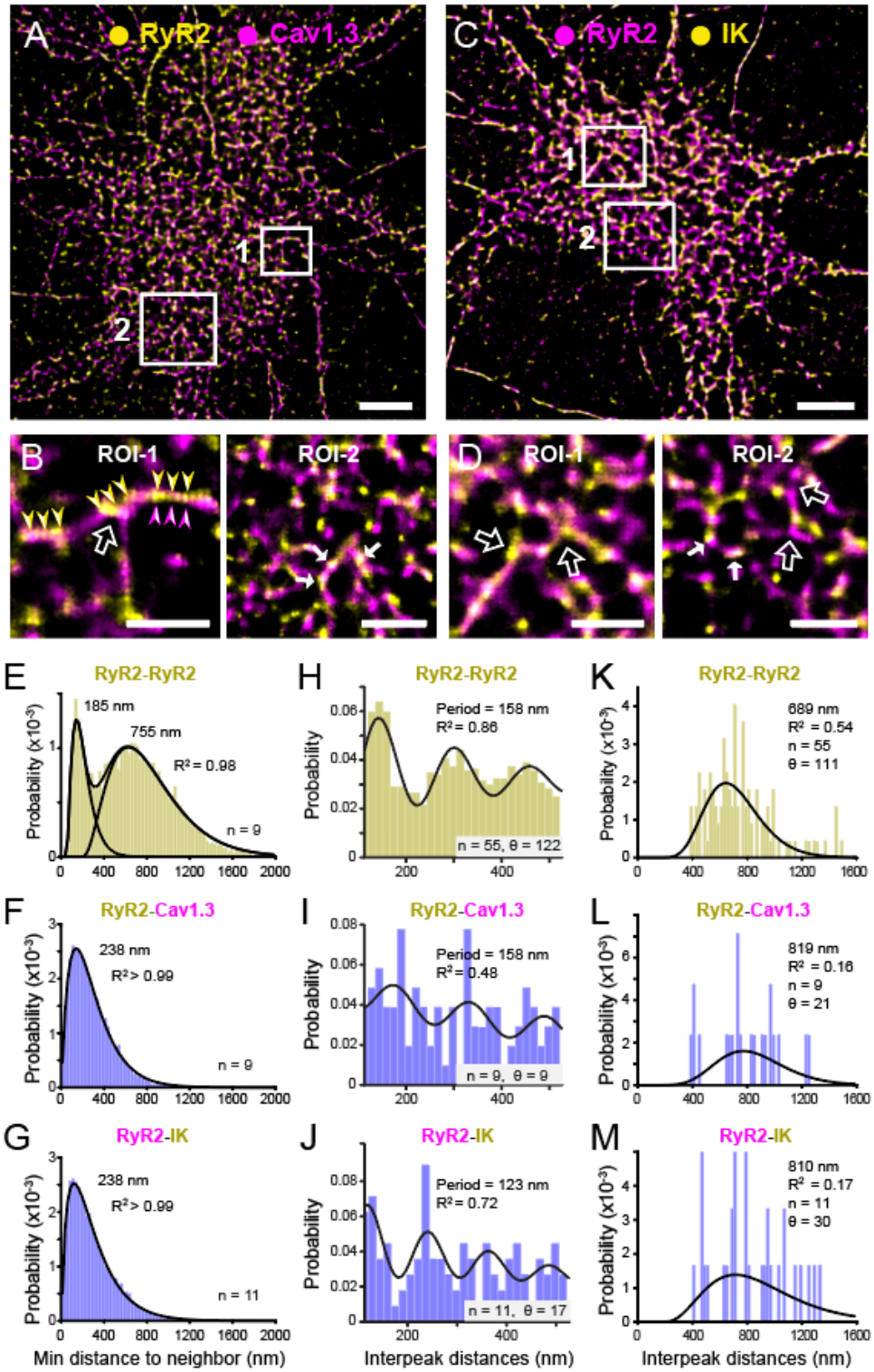

Figure 3. RyR2 exhibits a regular pattern of expression in relation to Cav1.3 and IK. (**A-D**) STORM-TIRF images of immunolabeled clusters for the indicated proteins. Larger field views (**A-C**) and magnified ROIs (**B-D**) show that RyR2 clusters exhibit an organized pattern in relation to Cav1.3 (**A-B**) or IK (**C-D**). RyR2 clusters are distributed in rows (**B,** ROI-1, *arrowheads*) that can reach branch points (**B-D,** *open arrows*) or be positioned in isolation. Cav1.3 and IK labels share these patterns and colocalize with RyR2 as rows of clusters (**B,** ROI-1, *arrowheads;* **B** and **D,** ROI-2, *filled arrows*) or as isolated labels. (**E-G**) NND analysis of dual labeled cells reveals two populations of distance between RyR2 clusters (**E**) and right-skewed single peaks for RyR2-Cav1.3 (**F**) or RyR2-IK (**G**). (**H-M**) NMF analysis defines a periodic pattern for colabeled cluster rows (**H-J**) or a single distribution for isolated clusters (**K-M**). Sample values (n) = cells, θ = features. Calibration bars: (**A-C**) 5 µm; (**B-D**) 2 µm. Bin widths: (**E-G**) 25 nm, (**H-J**) 15 nm, (**K-M**) 20 nm. See also ***Fig. S1, Supplemental Tables S1 and S2.***

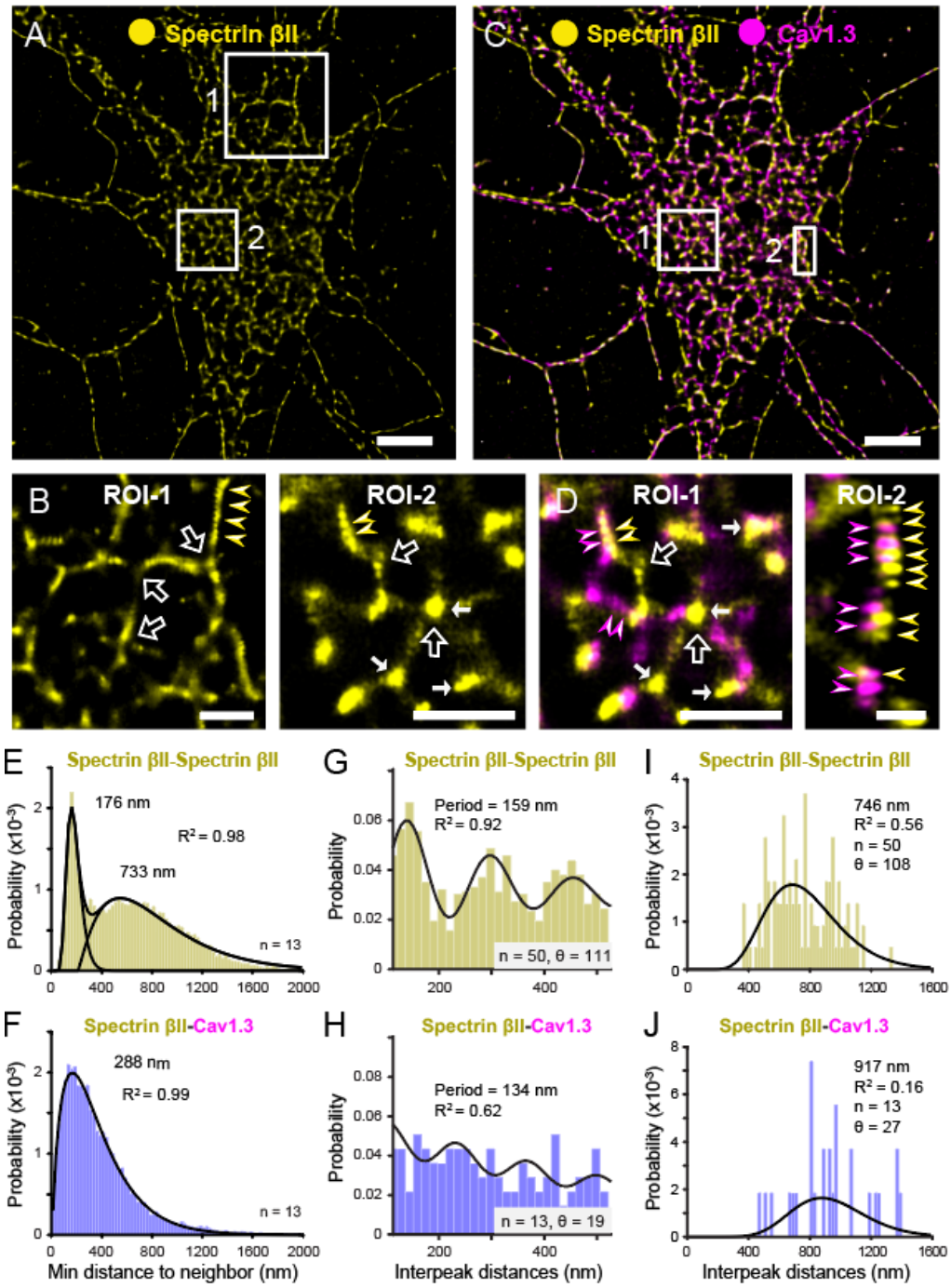

Figure 4. Spectrin βII exhibits a structured pattern associated with Cav1.3. (**A-D**) STORM-TIRF images of immunolabeled clusters for the indicated proteins. Shown are larger fields of view for a cell labeled for spectrin βII (**A** and **B**) and the same cell dual labeled for spectrin βII and Cav1.3 (**C** and **D**). ROIs are magnified in (**B** and **D**), with the same frame of view in (**B,** ROI-2) and (**D,** ROI-1). (**B** and **D**) Spectrin βII labeled clusters organize as rows of clusters (*arrowheads*) that extend to branch points (*open arrows*) or as isolated clusters (*filled arrows*). Dual labeling reveals Cav1.3 clusters that overlap with spectrin βII cluster rows (**C** and **D,** ROI-1, 2, *arrowheads*). (**E-F**) NND in dual labeled cells reveals two populations between spectrin βII clusters (**E**) and one for spectrin βII-Cav1.3 (**F**). (**G-J**) NMF analysis defines a periodic pattern for cluster rows (**G** and **H**) or a single distribution for isolated clusters (**I** and **J**). Sample values (n) = cells, θ = features. R^2 value in (**E**) corresponds to the superimposed combined fit for the two populations. Scale bars: (**A** and **C**) 5 µm; (**B,** ROI-1, -2; **D,** ROI-1), 2 µm; (**D,** ROI-2), 500 nm. Bin widths: (**E-F)** 25 nm, (**G-H**) 15 nm, (**I-J**) 20 nm. See also ***Supplemental Tables S1 and S2.***

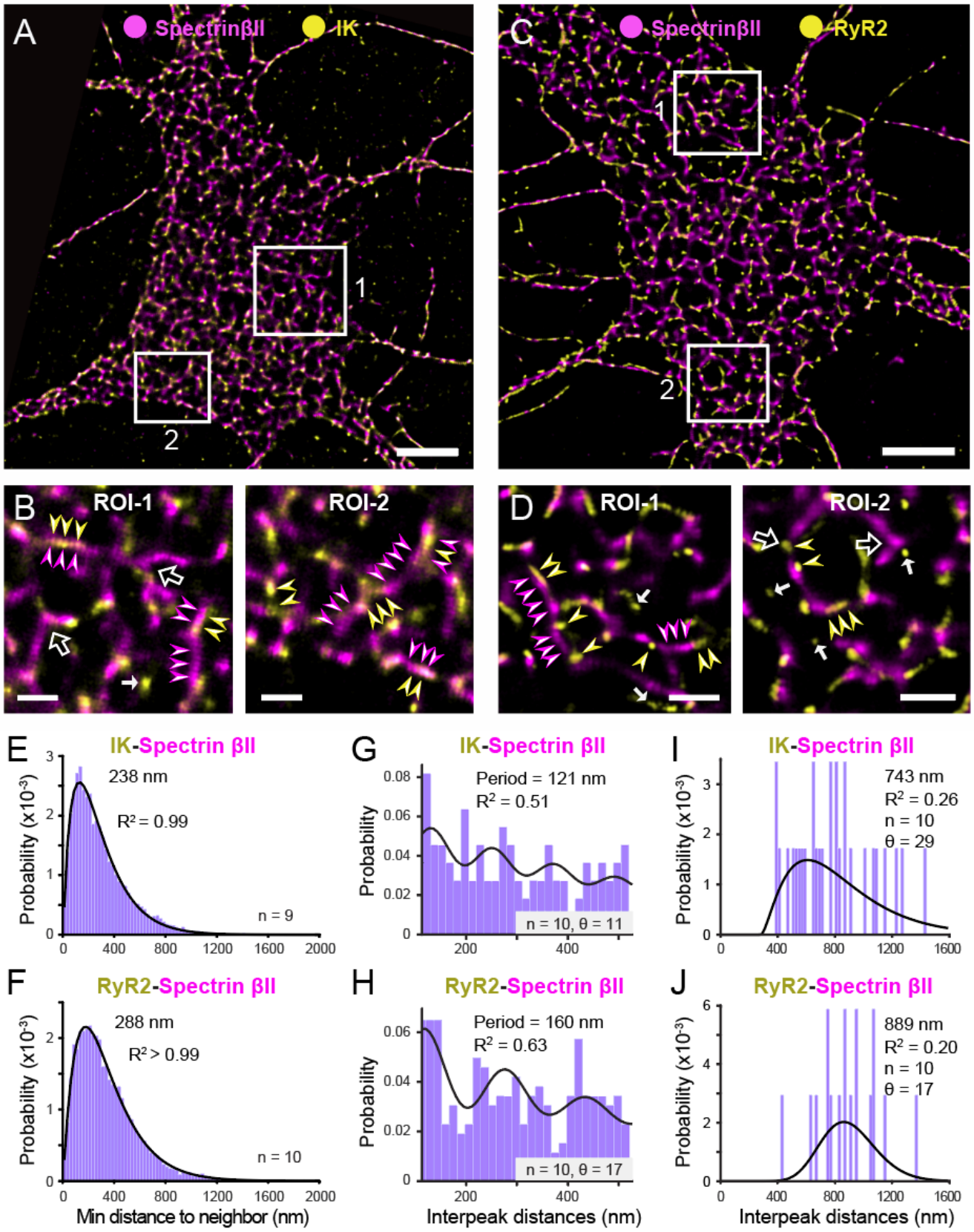
A
SpectrinβII
IK
1
2
C
SpectrinβII
RyR2
1
2
B
ROI-1
ROI-2
D
ROI-1
ROI-2
E
IK-Spectrin βII
238 nm
R² = 0.99
n = 9
Probability (x10⁻³)
F
RyR2-Spectrin βII
288 nm
R² > 0.99
n = 10
Probability (x10⁻³)
Min distance to neighbor (nm)
G
IK-Spectrin βII
Period = 121 nm
R² = 0.51
n = 10, θ = 11
Probability
H
RyR2-Spectrin βII
Period = 160 nm
R² = 0.63
n = 10, θ = 17
Probability
Interpeak distances (nm)
I
IK-Spectrin βII
743 nm
R² = 0.26
n = 10
θ = 29
Probability (x10⁻³)
J
RyR2-Spectrin βII
889 nm
R² = 0.20
n = 10
θ = 17
Probability (x10⁻³)
Interpeak distances (nm)

Figure 5. Spectrin exhibits an organized pattern that is closely associated with IK and RyR2 distributions. (**A-D**) STORM-TIRF images of immunolabeled clusters for the indicated proteins. Larger field views (**A** and **C**) with ROIs magnified (**B** and **D**) identify rows of spectrin βII clusters that can reach branch points (*open arrows*) that colocalize or alternate with rows of IK or RyR2 (*arrowheads*). Isolated clusters can be distinguished for IK or RyR2 (**B,** ROI-2, **D**, ROI-1, 2; *filled arrows*). (**E-F**) NND analysis between IK-spectrin βII (**E**) and RyR2-spectrin βII (**F**). (**G-J**), NMF analysis defines a periodic pattern for cluster rows (**G-H**) or a single distribution for isolated clusters (**I-J**). Sample values (n) = cells, θ = features. Scale bars: (**A** and **C**) 5 µm; (**B** and **D**, ROI-1, -2), 1 µm. Bin widths: (**E-F)** 25 nm, (**G-H**) 15 nm, (**I-J**) 20 nm. See also ***Fig. S7, Supplemental Table S1 and S2***.

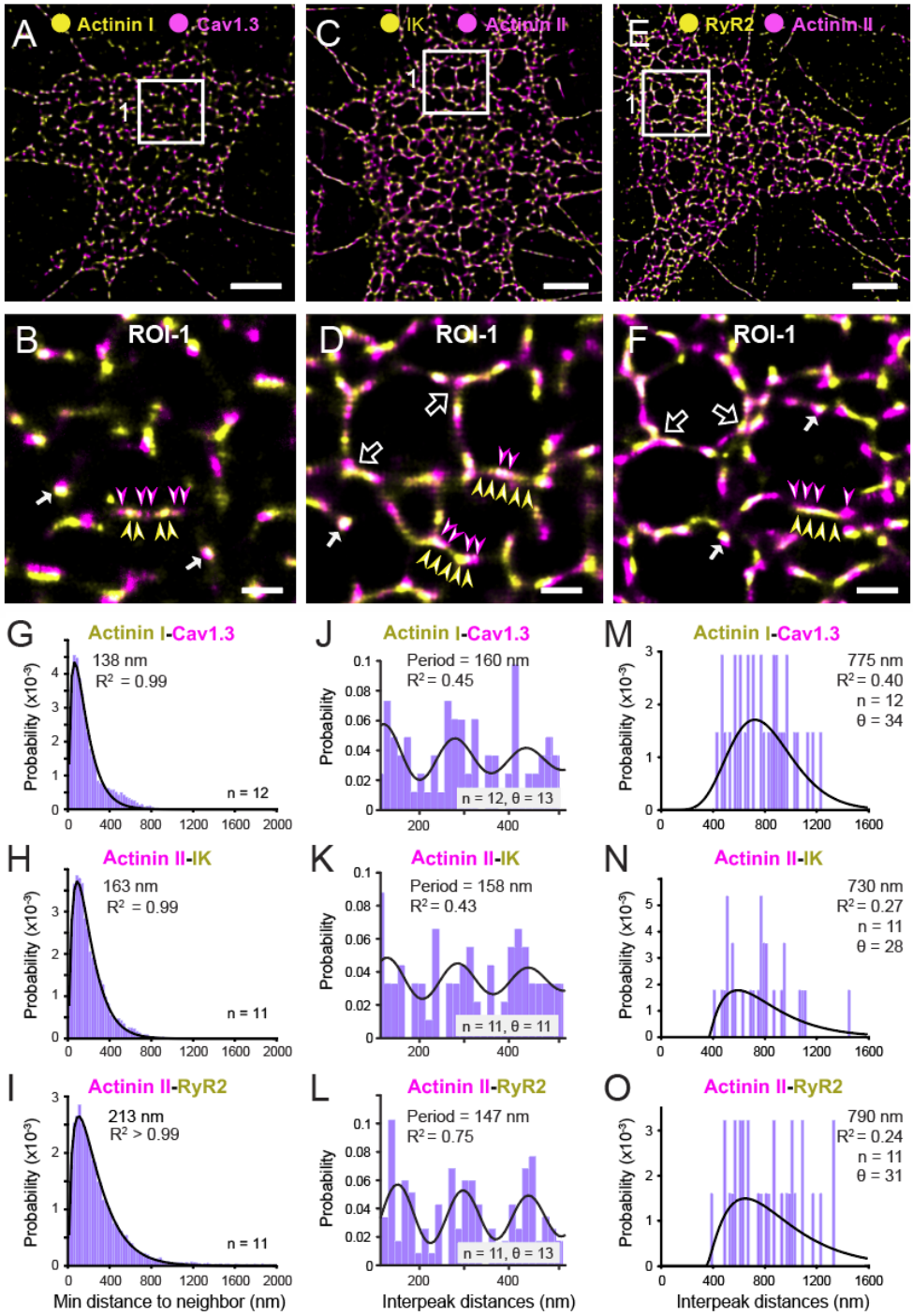

Figure 6. Actinin I and actinin II distributions are aligned with CaRyK complex proteins. (**A-F**) STORM-TIRF images of immunolabeled clusters for the indicated proteins. Shown are dual labeled images for the indicated CaRyK complex proteins and actinin isoforms. Larger field views (**A, C, E**) and associated ROIs (**B, D, F**) identify clusters that align in rows that either overlap or alternate (*arrowheads*) with actinin isoforms. Cluster rows can extend to branch points (*open arrows*), colocalize (*solid arrows*), or alternate to extend or bridge rows of labels (*arrowheads*). (**G-I**) NND analysis between actinin I - Cav1.3 (**G**), actinin II - IK (**H**) and actinin II - RyR2 (**I**). (**J-O**) NMF analysis defines a periodic pattern for cluster rows (**J-L**) or a single distribution for isolated clusters (**M-O**). Sample values (n) = cells, θ = features. Scale bars: (**A, C, E**) 5 µm; (**B, D, F**), 1 µm. Bin widths: (**G-I**) 25 nm, (**J-L**) 15 nm, (**M-O**) 20 nm. See also ***Figs. S8 and S9, Supplemental Tables S1 and S2.***

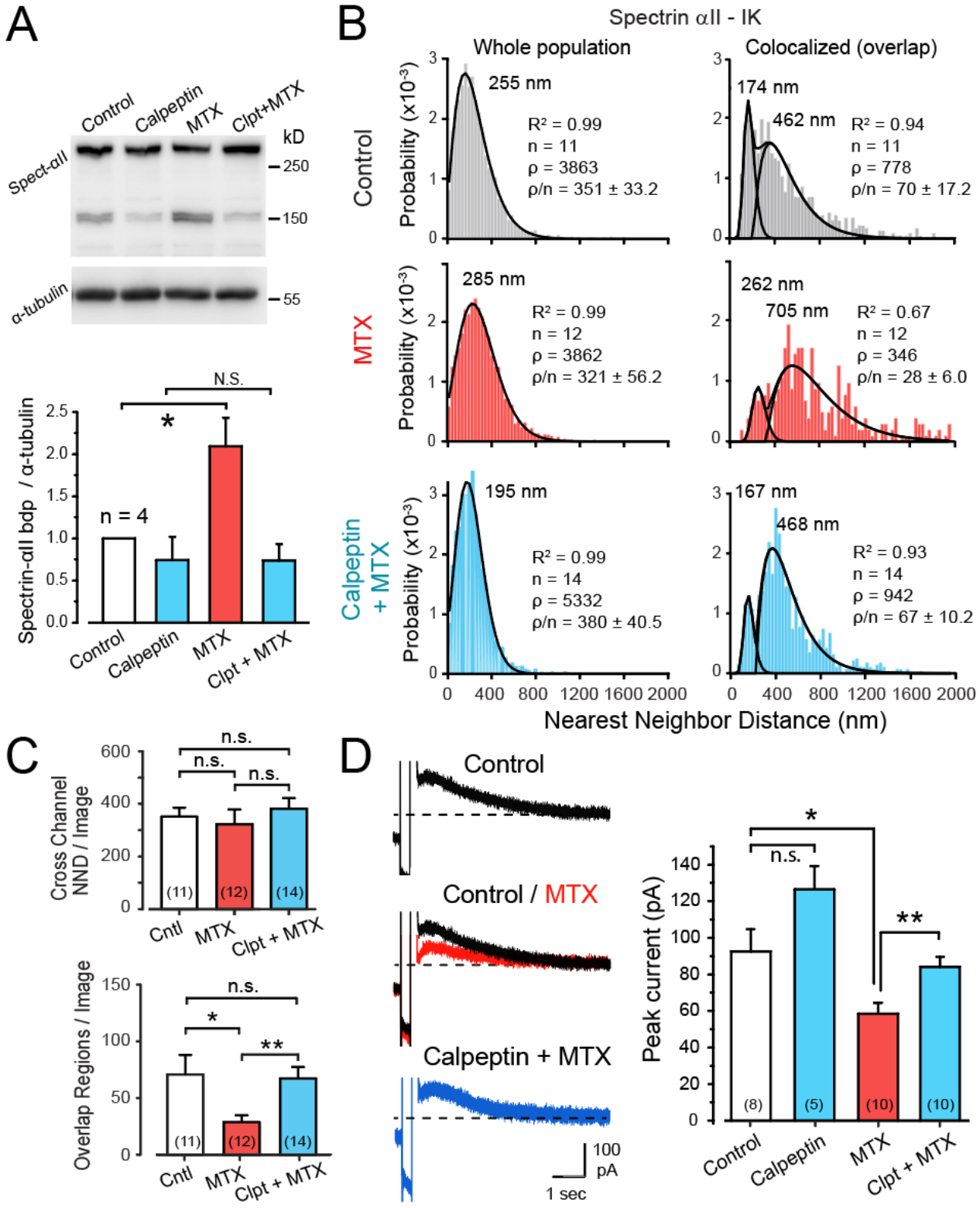

Figure 7. The sAHP of CA1 pyramidal cells depends on the integrity of the spectrin cytoskeleton. (**A**) Western blot analysis for spectrin αII in rat P21-26 hippocampal slices pretreated with control aCSF or 5 µM calpeptin for 3 hr, control aCSF (1 hr) and then 1 nM MTX (2 hr), or 5 µM calpeptin (Clpt, 1 hr) + MTX (2 hr). MTX induces breakdown products of spectrin αII at ~150 kDa that are reduced by calpeptin. Mean band

densities on Western blots are normalized to the levels of α-tubulin (n = 4). (**B**) Control NND plots for the whole population of clusters imaged in CA1 pyramidal cell somata of P20-25 rats returns a right skewed histogram (left), and for colocalized clusters (overlapping pixels) a dual exponential fit with median values that is equivalent to that of cultured cells (right). MTX treatment (80 pM, 1 hr) increases the median NND value at the population level and substantially alters the number (***ρ***) and median values of fits for distance between colocalized cluster centers, with values restored by pretreatment with calpeptin. (**C**) Mean bar plots of NND median values for data in (**B**) for the whole population or colocalized data sets under the indicated conditions. Comparison with Wilcoxon ranksum test. (**D**) Whole cell recordings of the IK-mediated IsAHP in CA1 pyramidal cells of P21-P26 rats. IsAHP was evoked by a step command from -100 mV to +40 mV (200 msec) and back to -50 mV. Currents are from cells recorded from control sections, after 1 hr 40 pM MTX, or when exposed to 5 µM calpeptin with or without 40 pM MTX. Mean bar plots of IsAHP amplitude are shown for the indicated conditions. Average values are mean ± S.E.M, Student's *t*-test; * $p < 0.05$; ** $p < 0.01$; N.S., not significant. Sample numbers are shown in brackets. ρ, number of centroids detected across all images for a given label set; ρ/n, mean centroids per cell; R^2 coefficient of determination for combined fit of two populations in (**B**). Bin width (**B**), 30 nm. See also ***Fig. S10 and Supplemental Table S1***.

Supplementary Materials for

A somatic afterhyperpolarization is driven by ion channel nodes across a Spectrin Polygonal Lattice

Giriraj Sahu *et al.*

This PDF file includes:

Fig. S1 to S10

Tables S1 to S5

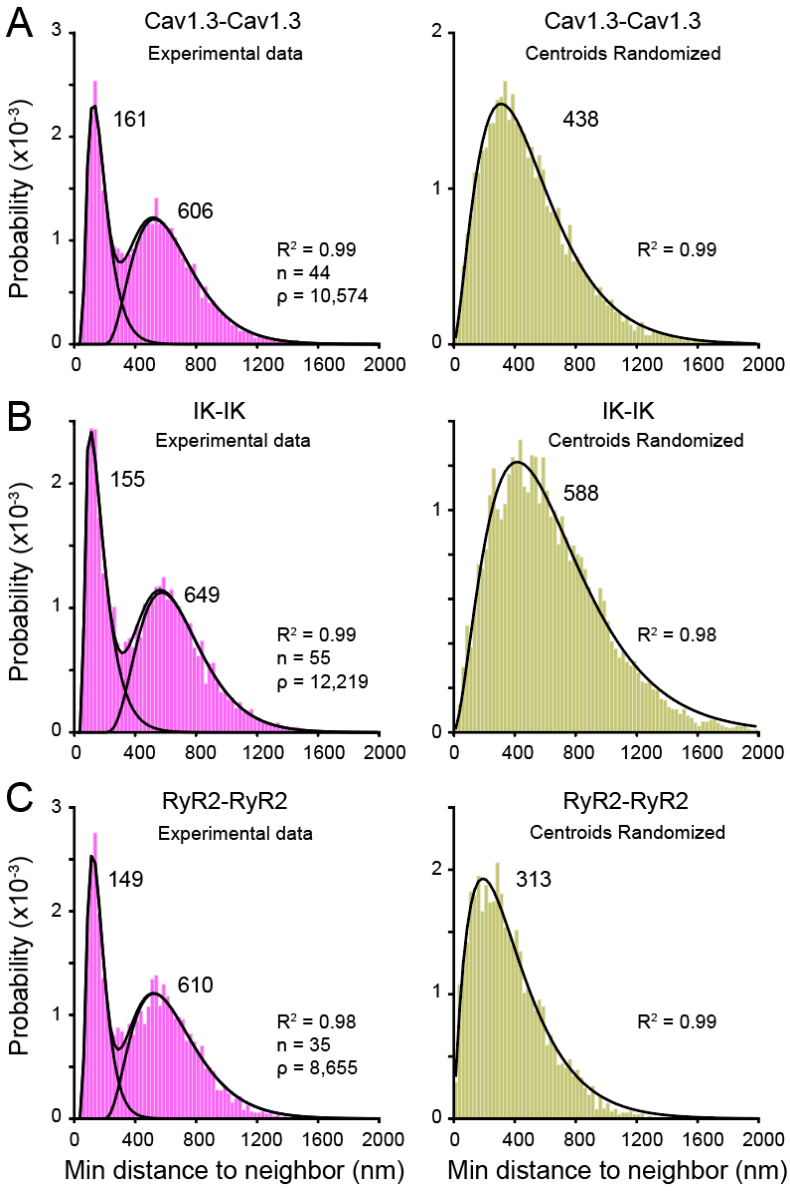

Figure S1. The spatial distribution of CaRyK protein clusters at the soma is dissimilar from a random shuffle. Related to ***Fig. 1 and 3***. (**A-C**) *Left column* provides NND distributions of the indicated CaRyK complex proteins. *Right column* indicates NND distributions for the same datasets after randomizing centroid positions. Significant differences exist between experimental and randomized data for each protein (non-parametric 2- sample Kolmogorov–Smirnov test (KS)): (**A**) $p < 0.001$, KS-stat = 0.1180; (**B**) $p < 0.001$, KS-stat = 0.1999; (**C**) $p < 0.001$, KS-stat = 0.1957). Numerical indicators adjacent to histograms represent median values. Sample values (n) = cells, ρ, number of centroids detected across all images for a given label set. Bin widths: (**A-C**) 25 nm.

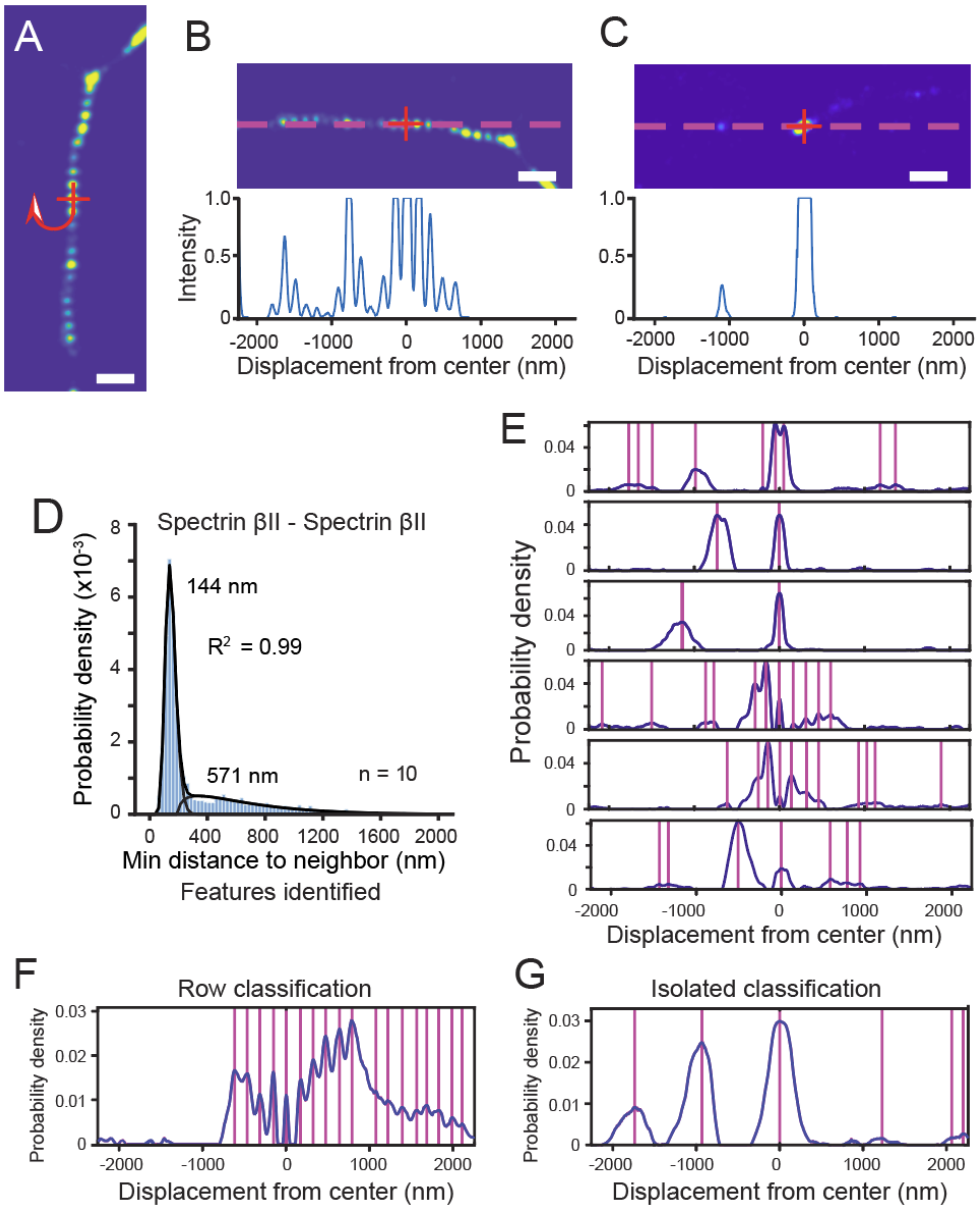

Figure S2. The use of NMF to define patterns in immunolabeled cluster centroids. (**A-C**) Procedure to define relationships between immunolabeled clusters in representative STORM-TIRF images of neuronal processes outside of the soma labeled for spectrin βII. A systematic pixel-by-pixel search identifies the center of a detected centroid (**A,** *cross*) for spectrin βII labeling. Images are then rotated to a position where its nearest neighboring centroid is oriented to the left and the ROI is stored for feature detection (**B-C**). Below the images in (**B-C**) are 1D displays of normalized pixel intensity aligned with the profile indicated by *dashed lines* for a row of clusters consistent with the MPS (**A-B**) as well as isolated clusters (**C**). (**D**) NND analysis of spectrin βII clusters in neuronal processes reveal two populations of inter cluster distances, with the majority fitting a distribution with a median value of 144 nm. (**E**) Representative example of centroid features extracted by NMF from spectrin βII labeled neural processes outside the soma of a single cell with k = 6. *Vertical lines* denote detected peak positions. (**F-G**) Two representative examples of features containing rows (**F**) or isolated clusters (**G**) for spectrin βII labeling. Scale bars: (**A-C**) 500 nm. Bin width (**D**) 25 nm.

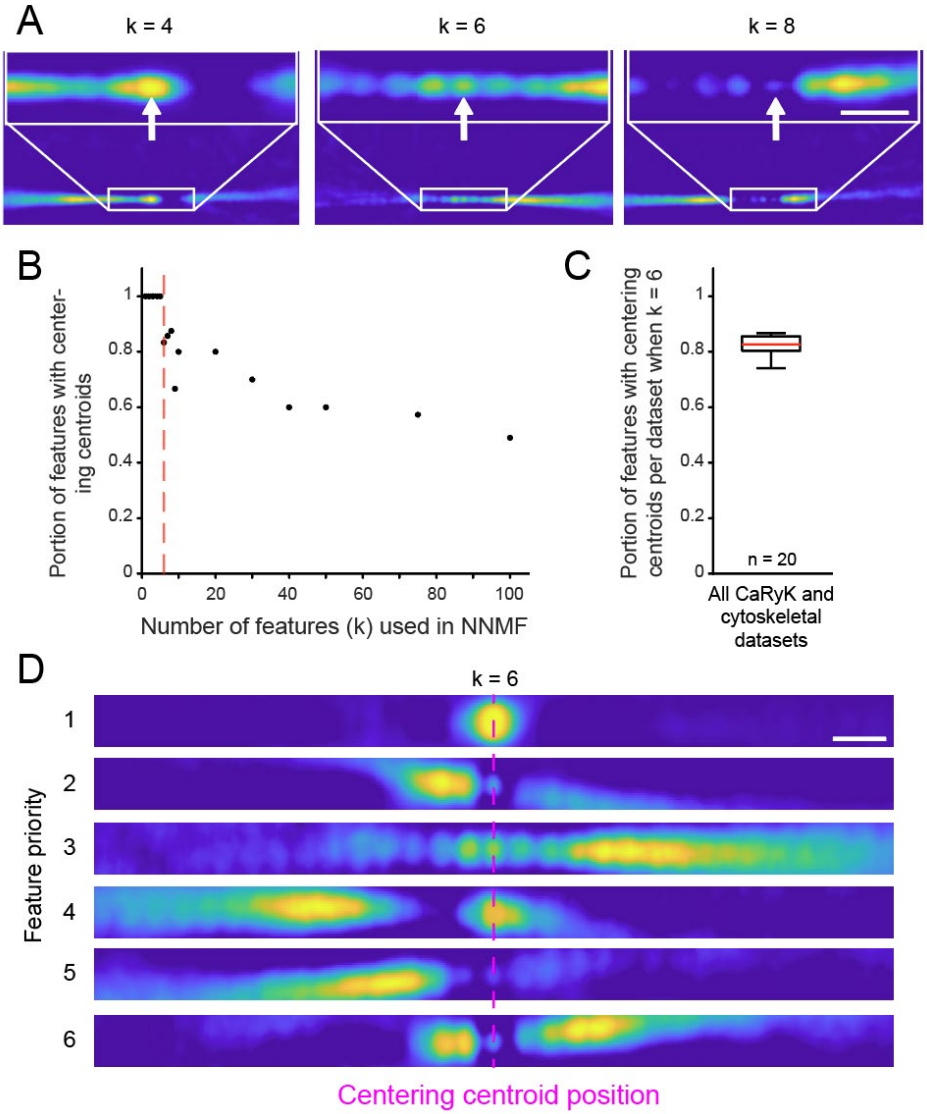

Figure S3. Rationale for feature number selection for NMF. The effects of using different numbers of features (k) to calculate the distance between rows of clusters using NMF. NMF generates features as rows of a matrix which are reported in decreasing importance to the original data set. Every cluster centroid image prior to input into NMF has a central point spread function upon which the image is aligned to identify intercluster distances of neighboring rows of clusters. (**A**) A representative case of feature detection for different k values for spectrin βII images, with each case illustrating the third feature calculated by NMF. ROIs of the regions indicated by a *white box* are shown expanded above. As k increases, attributes of each feature become diluted until the central centroid (*white* arrows) becomes diminished or is no more prominent than noise (i.e. k = 8). (**B**) Scatter plot showing a progressive loss of central centroids in downstream analysis as the number of features generated is increased. *Red dashed line* indicates k = 6 (portion = 0.8333). (**C**) Box plot of the portion of features across CaRyK, spectrin and actinin datasets which contain a detectable central centroid to calculate intercluster distances in rows of immunolabeled clusters (mean = 0.824 ± 0.0075). Analyses were conducted with k = 6 to avoid instances where the centering centroid was miniscule or absent and ensure that features reflected a plausible centroid image while maximizing the number of features for downstream analysis. (**D**) Representative example of the top six features extracted for spectrin βII in MAP2 positive or negative processes of hippocampal cells. Scale bars: (**A**, ROIs) 300 nm, (**D**) 300 nm. Sample values (n) in (**C**) reflect all data sets for CaRyK, spectrin and actinin immunolabels.

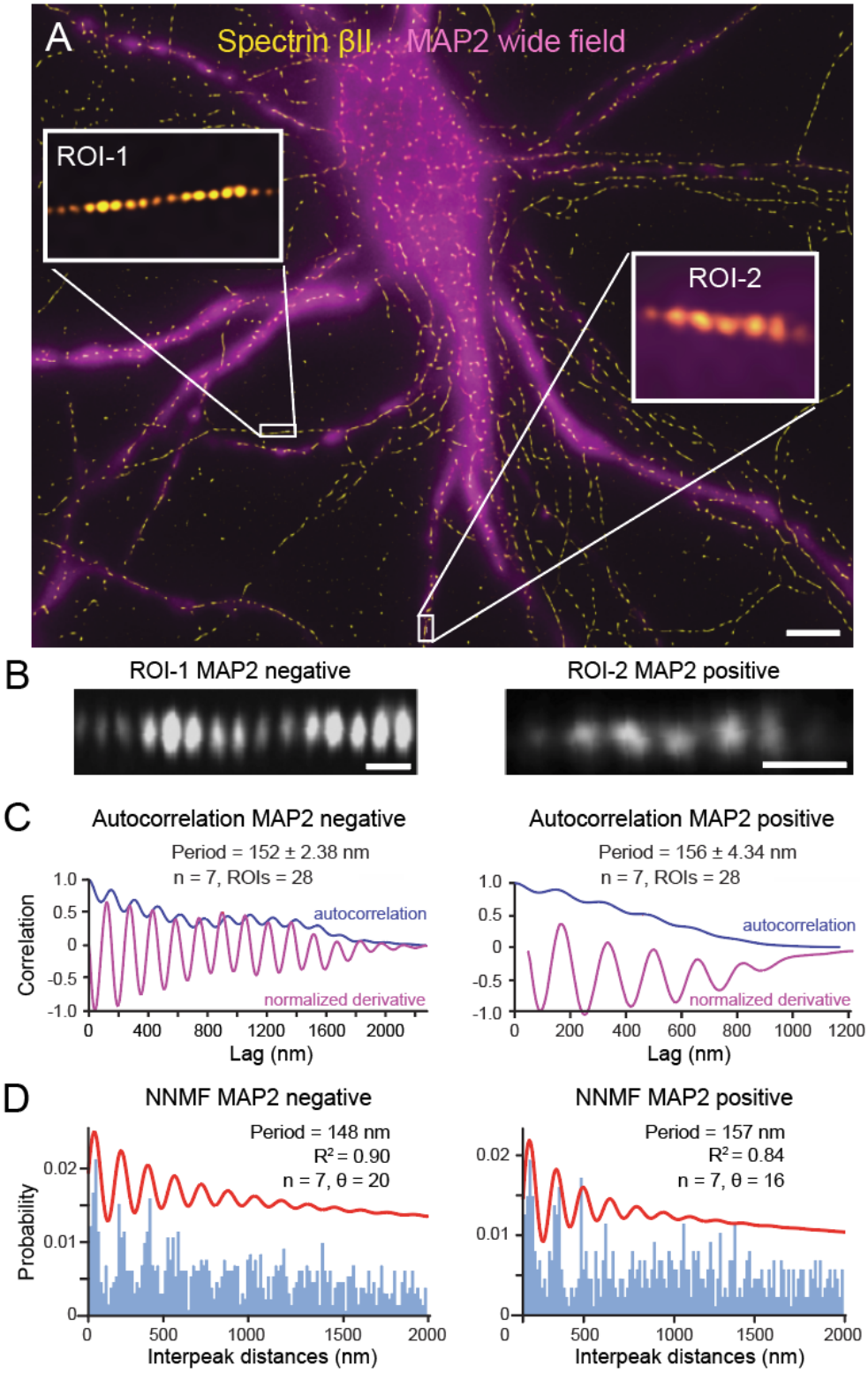

Figure S4. Comparison of periodicity in cluster organization measured by autocorrelation vs NMF. (**A-B**) Representative STORM-TIRF image of spectrin βII labeling with an overlaid larger field image of MAP2-GFP labeling (**A**). Two processes are highlighted as MAP2 negative putative axons (ROI-1) and MAP2 positive putative dendrites (ROI-2) (**B**). (**C-D**) Spectrin βII labeling of MAP2 negative or MAP2 positive processes outside of the soma are analyzed for periodicity by autocorrelation (**C**) or NMF (**D**). In (**C**) the autocorrelations (*blue lines*) and normalized derivatives (*magenta lines*) are shown superimposed and drawn from the specific ROI examples in (**B**), while mean periods are calculated from the entire population of clusters. In (**D**) histograms of interpeak distance of row classified spectrin βII features from the same data set are shown superimposed with the damped oscillatory model fits (*red lines*) calculated by NMF. Scale bars: (**A**) 5 µm, (**B,** ROI-1, 2) 300 nm. Average values are mean ± SEM. Sample values (n) = cells, θ = NMF row features (**E**). Bin widths: (**D**) 15.4 nm.

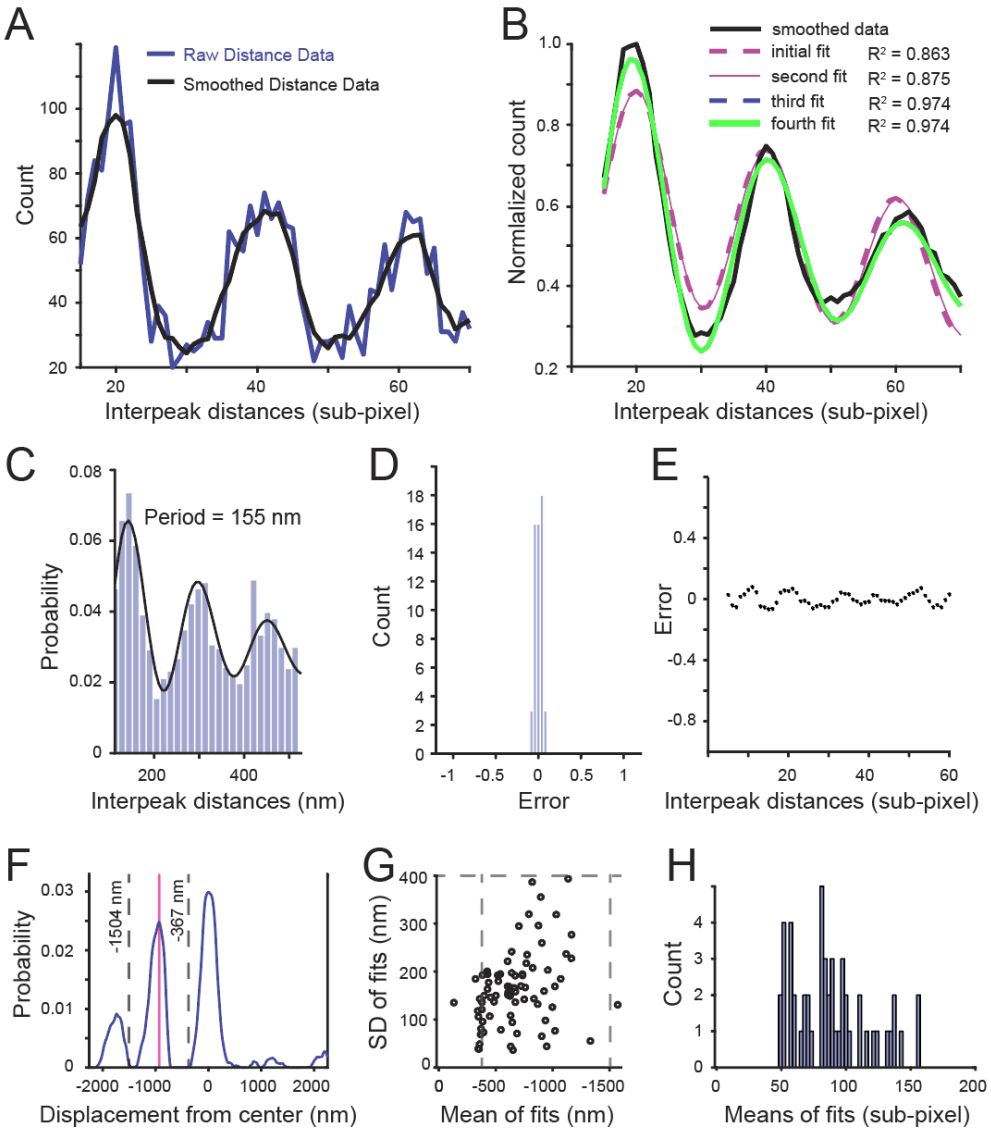

Figure S5. Defining inter cluster distances from NMF. Procedure for oscillatory model fitting of the NMF defined interpeak distance histograms. (**A**) Plot of the heights of binned interpeak distances of the initial 3 cycles of row classified features generated by NMF of spectrin βII labeled processes. Interpeak distances are cropped to a range of 15-70 sub-pixels to accommodate the highest S/N region. Shown superimposed is data before and after smoothing with a moving average to improve model fit. (**B**) Superimposed records of smoothed data trace from (**A**) fit with a damped oscillatory model for 4 iterations using a least-squares method. (**C-E**) Representative example of best fit model and error values for spectrin βII NMF calculations in processes, with the best fit model (*black line*) superimposed on the histogram of raw interpeak distance data in (**C**). Shown in (**D-E**) is the histogram of error between model and data (**D**), with error distributed around zero. A scatter plot of error along the X axis of data in (**C**) is relatively homoscedastic (**E**). (**F-H**) Procedure for defining peak centers of isolated features identified by NMF. A representative example of an isolated classified feature as a plot of probability in relation to distance from centering centroid for spectrin βII - spectrin βII (**F**). An examination window of -1504 to -367 nm (*gray dashed lines*) is used to avoid the influence of the centering centroid or distant data tails in defining the peak of isolated clusters (*magenta vertical line*) (**F**). (**G**) Data within the examination window is fit with a single gaussian. A plot of the mean and SD of fits of isolated cluster gaussians is used to confirm a single population of gaussians and eliminate outliers defined using *rmoutliers*. Any gaussians that fell outside of the examination window (*gray dashed lines*) were removed, along with gaussians that were not well fit to the data they represented ($R^2 \leq 0.9$). (**H**) Final histogram of accepted means for isolated cluster distances determined in (**F-G**). Bin widths: (**C**) 15 nm, (**D**) 0.04, (**H**) 20 nm.

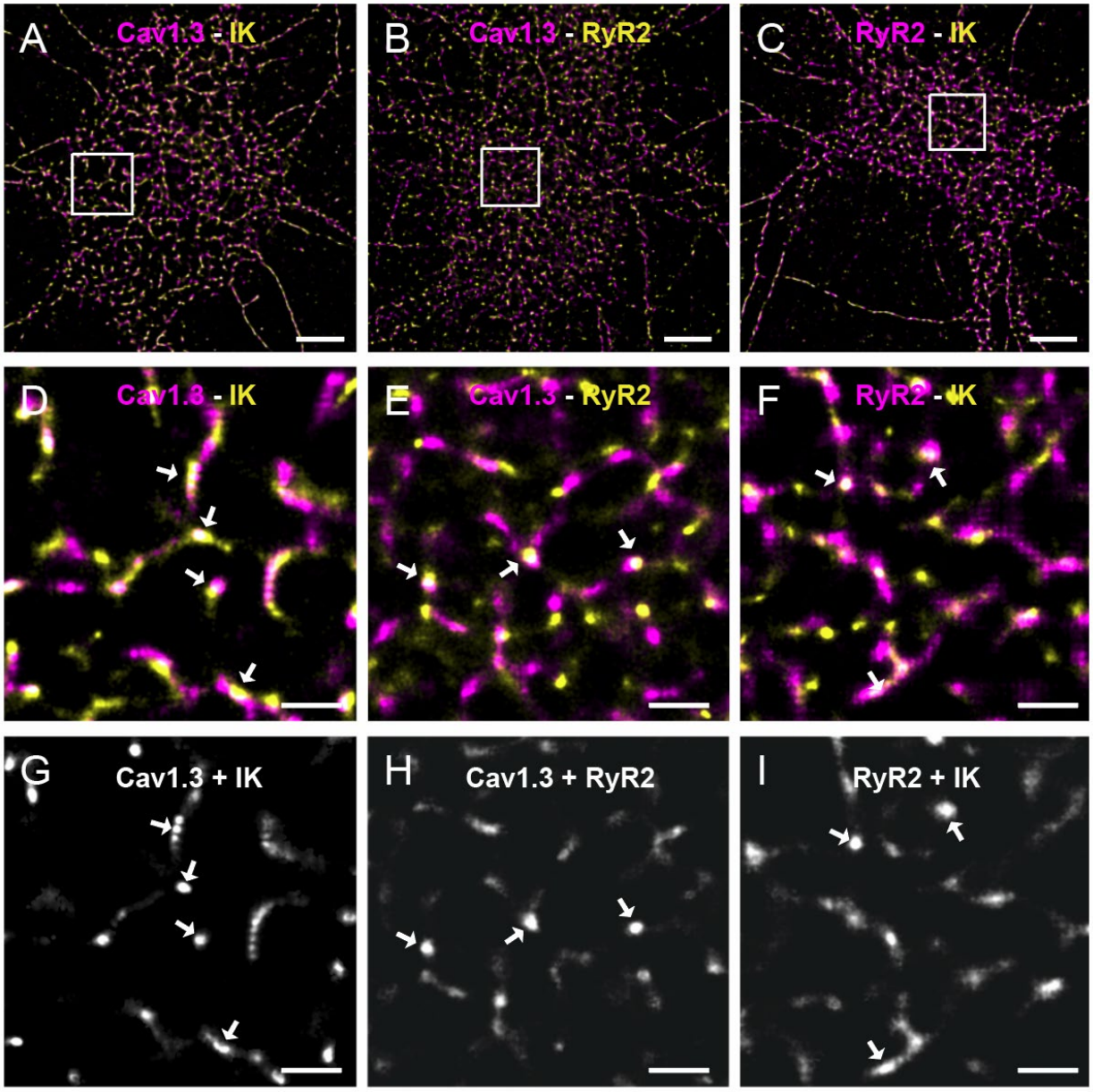

Figure S6. Generating images of fluorescent emission overlap for NMF analysis. Related to Fig. 1-6. (**A-C**) Larger field views of hippocampal neurons dual labeled for the indicated proteins. (**D-F**) Expanded views of ROIs from images in (**A-C**) illustrating overlap of some fluorescence emissions (white chroma, *arrows*) suggestive of protein colocalizations. (**G-I**) Black and white images of overlap-dependent intensity representations of the dual labels in (**D-F)** to apply NMF on dual labeled clusters. Pixel intensity of the overlap image is determined pixel wise by: $Overlap_{xy} = \sqrt{(Green\ Intensity_{xy})(Red\ Intensity_{xy})}$.

Scale bars: (**A-C**) 5 µm; (**D-I**), 500 nm. See also ***Supplemental Table S4.***

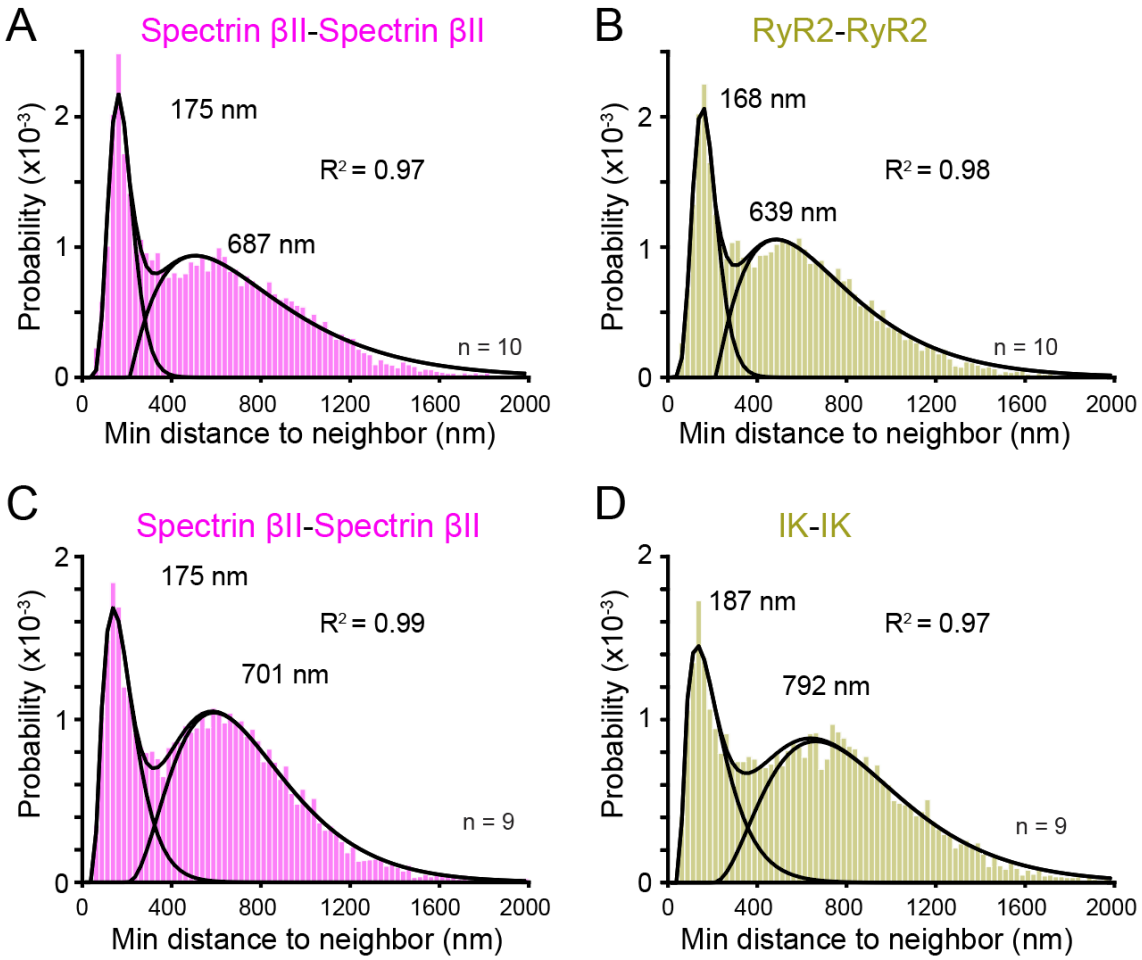

Figure S7.
Spectrin βII clusters distribute with similar patterns as IK and RyR2. ***Related to Fig. 4 and 5.*** (**A-D**) NND histograms of similar immunolabels in two sets of dual labeled tissue (**A-B,** spectrin βII-RyR2; **C-D,** spectrin βII-IK) reveals populations that can be described by two gamma fits. Values are the median of fit gamma distributions and R^2 of the combined fits. Sample values (n) represent the number of individual cells analyzed. Bin widths: 25 nm.

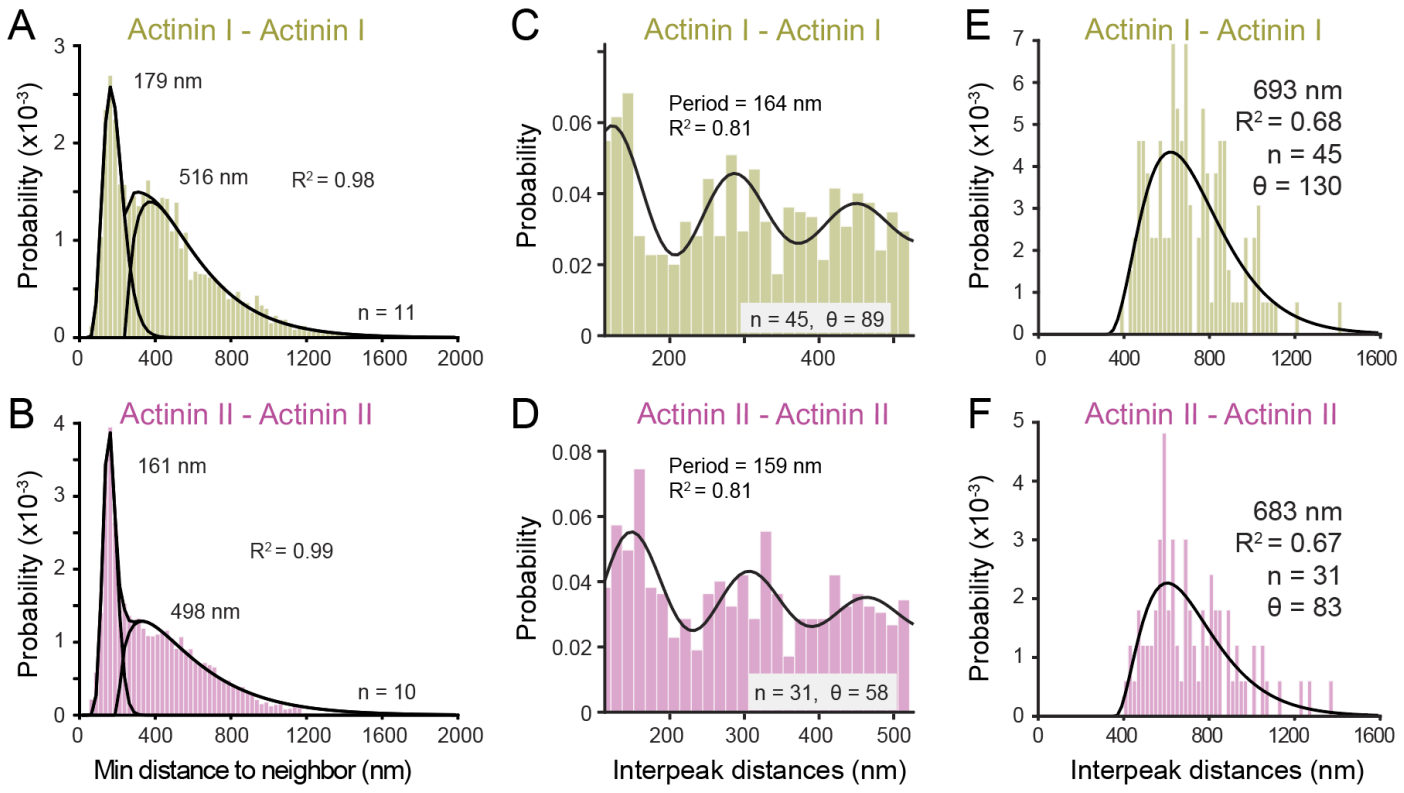

Figure S8. Actinin I and actinin II immunolabels exhibit a structured pattern indicative of rows and isolated clusters. Related to *Fig. 6.* (**A-B**) NND analysis within actinin I clusters (**A**) and actinin II clusters (**B**) reveal two populations of inter-centroid distance fit with two gamma distributions. Distributions are comparable to that of spectrin βII (see **Fig. 4 and S8**). (**C-F**) NMF analysis of the indicated immunolabels defines a regular periodicity of cluster rows (**C-D**) or isolated clusters (**E-F**). Medians of gamma distributions, R^2 values of fitted gamma distributions (**A, B, E,** and **F**), model periods and with their associated R^2 values (**C-D**) are indicated on plots. Total number of centroids detected to apply NMF (**C-F**): actinin I-actinin I, 19,767; actinin II-actinin II, 21,634. Sample values (n) = cells, θ = features. Bin widths: (**A-B)** 25 nm, (**C-D**) 15 nm, (**E-F**) 20 nm.

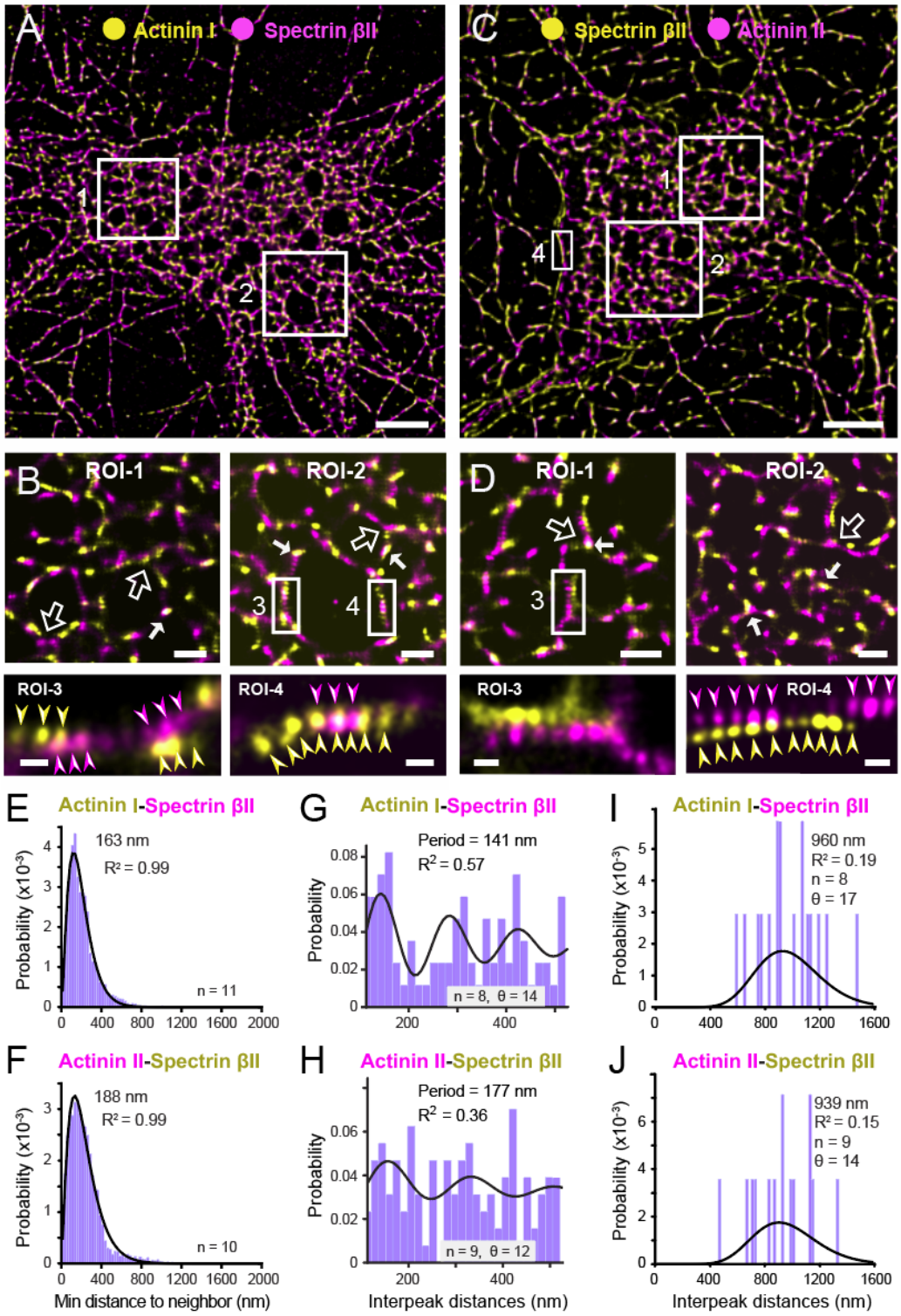

Figure S9. Actinin I and actinin II exhibit an organized pattern in relation to spectrin βII. ***Related to Figure 6.***

(**A-D**) STORM-TIRF images of immunolabeled clusters for the indicated proteins. Shown are dual labeled images for spectrin with actinin I (**A-B**) or with actinin II (**C-D**), with ROIs magnified in (**B** and **D**). Rows of spectrin βII or actinin clusters can extend to branch points (*open arrows*), colocalize (*solid arrows*), or alternate to extend or bridge rows of labels (*arrowheads*).

(**E-F**) NND analysis between actinin I-spectrin βII (**E**) and actinin II-spectrin βII (**F**).

(**G-J**) NMF analysis defines a periodic pattern for cluster rows (**G-H**) or a single distribution for isolated clusters (**I-J**). Sample values (n) = cells, θ = features. Scale bars: (**A** and **C**) 5 µm; (**B** and **D,** ROI-1, 2), 1 µm; (**B** and **D,** lower ROIs), 200 nm. Bin widths: (**E-F**) 25 nm, (**G-H**) 15 nm, (**I-J**) 20 nm. See also ***Supplemental Tables S1 and S2.***

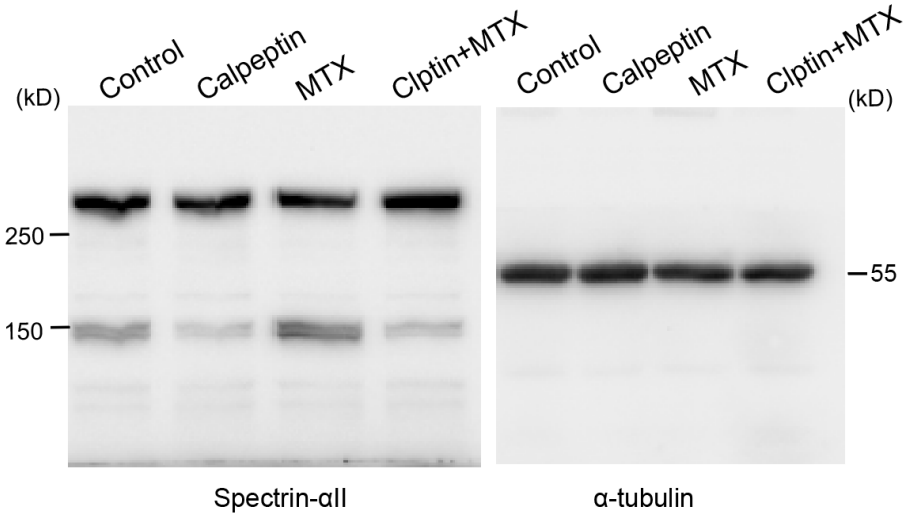

Figure S10. Maitotoxin activates calpain to proteolyze the spectrin cytoskeleton. ***Related to Figure 7.*** Full Western blots for spectrin αII in rat P21-26 hippocampal slices pretreated with in aCSF (control) or 5 µM calpeptin for 3 hr, control aCSF (1 hr) and then 1 nM MTX (2 hr), and 5 µM calpeptin (Clptin, 1 hr) + MTX (2 hr). Breakdown products for spectrin are apparent at ~150 kDa in all samples, but accentuated in MTX and reduced in the presence of calpeptin. Mean bar plots of band density are shown in ***Fig. 7A***.

Dual Labeled Tissue	Cluster Pairs	n	First Median (nm)	Second Median (nm)	R^2	Mixing % of first gamma in GMM
Cav1.3 - IK	Cav1.3 -Cav1.3	11	169	664	0.9773	27.2
	IK-IK		177	699	0.9827	27.7
	Cav1.3-IK		188	-	0.9935	100
IK - RyR2	IK - IK	11	186	722	0.9822	28.1
	RyR2 - RyR2		169	635	0.9888	33.2
	IK - RyR2		238	-	0.9973	100
Cav1.3 - RyR2	Cav1.3 - Cav1.3	9	174	624	0.9904	34.8
	RyR2 - RyR2		185	755	0.9822	25.1
	Cav1.3 - RyR2		238	-	0.9978	100
Cav1.3 - Spectrin βII	Cav1.3 - Cav1.3	13	168	649	0.9854	30.3
	Spectrin βII - Spectrin βII		183	733	0.9783	26.8
	Cav1.3 - Spectrin βII		288	-	0.9955	100
IK - Spectrin βII	IK - IK	9	187	792	0.9718	31.8
	Spectrin βII - Spectrin βII		175	701	0.9879	31.1
	IK - Spectrin βII		238	-	0.9939	100
RyR2 - Spectrin βII	RyR2 - RyR2	10	168	639	0.9854	28.9
	Spectrin βII - Spectrin βII		175	687	0.9720	29.4
	RyR2 - Spectrin βII		288	-	0.9959	100
Cav1.3 - Actinin I	Cav1.3 - Cav1.3	12	180	641	0.9902	23.2
	Actinin I- Actinin I		192	667	0.9870	18.2

	Cav1.3 - Actinin I		138	-	0.9880	100
IK - Actinin I	IK - IK	11	164	729	0.9872	27.7
	Actinin I - Actinin I		174	683	0.9757	27.6
	IK - Actinin I		363	-	0.9945	100
RyR2 - Actinin I	RyR2 - RyR2	10	168	704	0.9773	24.9
	Actinin I - Actinin I		179	718	0.9790	21.2
	RyR2 - Actinin I		338	-	0.9931	100
Spectrin βII - Actinin I	SpectrinβII - SpectrinβII	9	170	489	0.9812	27.6
	Actinin I - Actinin I		179	516	0.9780	30.0
	SpectrinβII - Actinin I		163	-	0.9859	100
IK- Actinin II	IK- IK	11	218	726	0.9800	42.5
	Actinin II- Actinin II		169	611	0.9901	34.2
	IK- Actinin II		163	-	0.9922	100
RyR2- Actinin II	RyR2- RyR2	10	186	730	0.9799	24.9
	Actinin II - Actinin II		166	628	0.9822	29.1
	RyR2- Actinin II		213	-	0.9966	100
Spectrin βII - Actinin II	SpectrinβII - SpectrinβII	10	161	498	0.9903	35.0
	Actinin II - Actinin II		161	452	0.9807	34.9
	SpectrinβII - Actinin II		188	-	0.9886	100
STED data						
Control Spectrin αII - IK	Spectrin αII - IK (overlap)	11	174	462	0.9396	28.6
	Spectrin αII - IK		225	-	0.9932	100
Maitotoxin 80 pM	Spectrin αII - IK (overlap)	12	262	705	0.6669	14.7

Spectrin αII - IK	Spectrin αII - IK		285	-	0.9939	100
Maitotoxin 80 pM with Calpeptin 5 μM Spectrin αII - IK	Spectrin αII -IK (overlap)	14	167	468	0.9269	14.8
	Spectrin αII - IK		195	-	0.9918	100

Supplemental Table S1. Summary comparisons of fitted gamma mixture models on NND for the indicated protein pairs. All cells were imaged with two immunolabel targets and NND distributions calculated for all clusters. NND was calculated using LAMA's morphological cluster analysis and fitted with a mixed gamma model to define central tendency for each gamma distribution in NND histograms**.** Cluster pairs = the labeled targets which are being compared to generate the NND histogram. n = the number of cells. R^2 = coefficient of determination when comparing the sum of fitted gamma distributions to the NND histogram. GMM = gamma-mixture model.

				Row Cluster Data			Isolated Cluster Data	
Dataset	**n**	**Centroids x10^3**	**θ**	**Period (nm)**	**R^2**	**SSQ**	**Median (nm)**	**R^2**
Cav1.3 - Cav1.3	45	36.8	270	159	0.846	0.221	638	0.733
IK - IK	53	32.7	318	139	0.873	0.127	714	0.653
RyR2 - RyR2	55	43.1	330	158	0.861	0.172	711	0.543
Spectrin βII - Spectrin βII	50	34.4	300	159	0.920	0.121	774	0.558
Actinin I - Actinin I	45	19.8	270	164	0.810	0.230	693	0.681
Actinin II - Actinin II	31	21.6	186	159	0.813	0.225	683	0.674
Cav1.3 - IK	11	4.1	66	156	0.647	0.612	795	0.308
Cav1.3 - RyR2	9	3.1	54	158	0.484	0.999	819	0.165
RyR2 - IK	11	4.4	66	123	0.724	0.497	810	0.170
Cav1.3 - Spectrin βII	13	5.6	78	134	0.625	0.404	917	0.165
RyR2 - Spectrin βII	10	3.3	60	160	0.626	0.508	889	0.203
Spectrin βII - IK	10	6.4	60	121	0.509	0.710	743	0.263
Cav1.3 - Actinin I	12	4.2	72	160	0.453	1.053	775	0.396
IK - Actinin I	11	3.5	66	171	0.529	0.791	906	0.141
RyR2 - Actinin I	14	3.1	84	159	0.743	0.447	868	0.382
Spectrin βII - Actinin I	8	6.3	48	141	0.574	0.983	960	0.192
Actinin II - IK	11	7.9	66	158	0.431	0.931	730	0.227
Actinin II -RyR2	11	4.1	66	147	0.754	0.740	790	0.238
Actinin II -Spectrin βII	9	4.7	54	177	0.356	1.027	939	0.154

Supplemental Table S2. Summary of NMF feature analysis for the indicated protein pairs. Information about data entered into the NMF workflow and the results. n = the number of cells imaged. Centroids = the sum of weighted positions across all images that were assessed by NMF to generate features. Θ = the number of features generated per label set. Row Cluster Data = features from NMF which were assessed for peak density anticipated in regular and repeating clusters. Isolated Cluster Data = features from NMF which were assessed with a low peak density anticipated by isolated centroids. Period = period of fitted damped oscillatory model on interpeak data from features. R^2 = coefficient of determination when comparing data to the fitted model. SSQ = sum of squared error between smoothed interpeak data and the fitted model. Median

center = displacement of fitted gamma on isolated features from their reference position. Empty cells represent instances where no interpretable data was produced.

	Welch 2 sample T-test			KS-test	
Angle comparisons	**t-stat**	**df**	**p-value**	**k-stat**	**p-value**
Cav1.3 - IK	-0.5008	197.16	0.6171	0.0925	0.7758
Cav1.3 - RyR2	0.2621	201	0.7935	0.0884	0.8232
IK - RyR2	0.7878	194.07	0.4318	0.1224	0.4392
Spectrin βII - Cav1.3	0.5033	208.84	0.6153	0.0813	0.8836
Spectrin βII - IK	1.0333	196.39	0.3027	0.1219	0.4321
Spectrin βII - RyR2	0.2486	201.87	0.8039	0.0577	0.9958
Spectrin βII - Actinin I	-1.378	214.27	0.1697	0.1141	0.4628
Spectrin βII - Actinin II	-0.2847	105.57	0.7764	0.0962	0.8982
Actinin I - Cav1.3	-0.8699	215.32	0.3853	0.0924	0.7313
Actinin I - IK	-0.4210	219	0.6742	0.0947	0.7088
Actinin I - RyR2	-1.149	212.22	0.2519	0.1133	0.4852
Actinin II - Cav1.3	0.1312	102.41	0.8959	0.0812	0.9571
Actinin II - IK	0.5372	88.523	0.5924	0.0851	0.9648
Actinin II - RyR2	-0.0825	100.95	0.9344	0.1115	0.7387

Supplemental Table S3. The distribution of cluster row branchpoint angles are not significantly different. With sample size > 100 normality assumption was ignored and Welch 2 sample t-test was used to compare the central tendency of distributions. Two sample Kolmogorov-smirnov (KS) test was used to test the null hypothesis of the distributions being from the same population. Statistical calculations were completed using R software. df, degrees of freedom.

A	B	n	% Overlap on (A)	% Overlap on (B)
Cav1.3	IK	11	22.5 ± 1.5	20.4 ± 1.9
RyR2	IK	11	13.0 ± 1.8	18.2 ± 1.7
Cav1.3	RyR2	9	9.6 ± 1.1	16.2 ± 1.6

Supplemental Table S4. Percent overlap of pixels labeled for CaRyK complex proteins in STORM-TIRF imaging. Dual labeled images were masked to their ROIs, thresholded at > 20% maximal intensity and all pixels were counted. When pixels in the same position in both channels were greater than the threshold, they were counted as overlapped and divided by the sum of pixels greater than threshold in each channel. Calculated in MATLAB with custom scripts.

REAGENT	SOURCE	IDENTIFIER
Primary Antibodies		
Rabbit polyclonal anti-Cav1.3 (1:250)	Alomone Labs	ACC-005; RRID:AB_2039775
Mouse monoclonal anti-Cav1.3 (1:250)	Novus Biol.	NBP2-12893; RRID:AB_2687841
Mouse monoclonal anti-KCa3.1 (1:250)	Santa Cruz	SC-365265; RRID:AB_10841432
Rabbit polyclonal anti-KCNN4 (1:250)	Abcam	ab215990; RRID:AB_3714743
Mouse monoclonal anti-RyR2 (C3-33) (1:200)	Sigma-Aldrich	R-128; RRID:AB_261301
Rabbit polyclonal anti-RyR2 (1:200)	Sigma-Aldrich	SAB4502707; RRID:AB_10746831
Rabbit polyclonal anti-Spectrin βII (1:250)	Abcam	AB264177; RRID:AB_1270902
Mouse monoclonal anti-Spectrin βII (1:250)	BD Transduction	612563; RRID:AB_399854
Mouse monoclonal anti-Spectrin αII (1:200)	Abcam	Ab11755; RRID:AB 298540
Goat polyclonal anti-Actinin I (1:250)	Novus Biol.	AF8279; RRID: AB_2922129
Rabbit monoclonal anti-Actinin II (1:250)	Abcam	ab72239; RRID:AB_1270902
Rabbit monoclonal anti-Actinin-II (1:250)	Abcam	ab68167; RRID:AB_11157538
Chicken polyclonal anti-MAP2 (1:500)	Abcam	ab5932; RRID:AB_92147
Monoclonal anti-rat CD11b/c microbeads	Miltenyi Biotec	130-105-634; RRID:AB_2783886
GLAST (ACSA-1)-biotin microbeads	Miltenyi Biotec	130-095-826; RRID: AB_2733472
Secondary Antibodies		
Goat F(ab´)$_2$ anti-rabbit IgG–Alexa Flour-647 (1:1000)	Jackson	111-606-047; RRID:AB_2338082
Rabbit F(ab´)$_2$ anti-mouse IgG–Cy3 (1:1000)	Jackson	315-166-047; RRID:AB_2340148
Rabbit F(ab´)$_2$ anti-chicken IgG–Alexa Fluor-488 (1:1000)	Jackson	303-546-003; RRID:AB_2339330
Donkey F(ab') anti-rabbit IgG–Alexa Fluor-64 (1:1000)	Jackson	711-606-152; RRID:AB_2340625
Goat anti-Mouse STAR 635P (1:200)	Abberior	ST635P-1001-500UG; RRID:AB_2893232
Goat anti-rabbit STAR Orange (1:200)	Abberior	STORANGE-1002-500UG; RRID:AB_3068622
Goat F(ab') anti-mouse IgG–Cy3 (1:1000)	Jackson	115-166-146; RRID:AB_2338708
Donkey F(ab') anti-goat IgG–Cy3 (1:1000)	Jackson	705-166-147; RRID:AB_2340413
Goat anti-chicken IgY (H+L) - Alexa Fluor 488 (1:600)	Abcam	ab150169; RRID:AB_2636803
HRP conjugated goat anti-mouse IgG (H+L) (1:3000)	Invitrogen	62-6520; RRID: AB_2533947
HRP conjugated donkey anti-rabbit IgG (1:5000)	Cytiva	NA9340; RRID: AB_772191
Chemicals, peptides, and recombinant proteins		
Isoflurane	Fresenius Kabi	Cat No. CP0406V2
Papain	Worthington	Cat No. LK003150
Dubecco's PBS	Sigma Aldrich	Cat No. D8537-500ML
Bovine Serum Albumin	Vector Labs.	Cat No. SP-5050
Normal Goat Serum	Jackson	Cat No. 005-000-121
Glucose oxidase (Aspergellius Niger)	Sigma Aldrich	Cat No. G2133-50KU
Catalase (Bovine)	Sigma Aldrich	Cat No. C3155-50MG
Beta-Mercaptoethanol	Sigma Aldrich	Cat No. M6250-100ML
Triton-X	Sigma Aldrich	Cat No. T-8787
Poly-L-Lysine	Sigma Aldrich	Cat No. P-7280
Neurobasal Medium	Invitrogen	Cat No. 21010-046
Pyruvate	Invitrogen	Cat No. 11360-070

Glutamine	Invitrogen	Cat No. 25030-081
B-27	Invitrogen	Cat No. 17504-044
Pen-Streptomycin	Invitrogen	Cat No. 15140-122
Laminin	Sigma Aldrich	Cat No. L2020
FBS	Gibco	Cat No. 26140-079
HEPES	Sigma Aldrich	Cat No. H3375
Glucose	Sigma Aldrich	Cat No. G8270
TetraSpek™ beads (100 nm diameter)	ThermoFisher	Cat No. T7279
MACS BSA solution	Miltenyi Biotec	Cat No. 130-091-376
Maitotoxin	BOC Sciences	Cat N. 59392-53-9
Calpeptin	ThermoFisher	CAS:117591-20-5
Other		
No. 1.5 18 mm Coverslip	Electron Microscopy Sci.	Cat No. 72222-01
70 µm separation filter	Corning	Cat No. 07201431
Minimacs Separator	Miltenyi Biotec	Cat No. 130-042-102
MACS Multi Stand	Miltenyi Biotec	Cat No. 130-042-303
MS Column	Miltenyi Biotec	Cat No. 130-042-201
Software and algorithms	Miltenyi Biotec	Cat No. 130-042-201
Fiji	(Schindelin *et al*, 2012)	https://imagej.net/Fiji
LAMA (17.07)	(Malkusch & Heilemann, 2016)	https://www.uni-frankfurt.de/54258347/Software
Adobe Illustrator CS6	Adobe	https://www.adobe.com/ca/products/illustrator.html
Matlab (R2022b)	Mathworks	https://www.mathworks.com/products/matlab.html
Huygen's Professional (25.04.0p2 64b)	Scientific Volume Imaging	http://svi.nl
Origin 8	Origin Lab	https://www.originlab.com/index.aspx?go=PRODUCTS/Origin
Deposited Data		
MATLAB Scripts	This study	https://doi.org/10.20383/103.01618
Data for MATLAB Scripts	This study	https://doi.org/10.20383/103.01618
Core Resources		
Live Cell Imaging Laboratory	UCalgary	RRID: SCR_024748

Supplemental Table S5. List of reagents and supplies used, software applications, and location of data repository.

References:

Malkusch S & Heilemann M (2016) Extracting quantitative information from single-molecule super-resolution imaging data with LAMA - LocAlization Microscopy Analyzer. *Sci Rep* 6: 34486

Schindelin J, Arganda-Carreras I, Frise E, Kaynig V, Longair M, Pietzsch T, Preibisch S, Rueden C, Saalfeld S, Schmid B, *et al* (2012) Fiji: an open-source platform for biological-image analysis. *Nat Methods* 9: 676–682